Article

Mesoporous Silica Nanoparticles as pH-Responsive Carrier for the Immune-Activating Drug Resiquimod Enhance the Local Immune Response in Mice

WAGNER, Julia, *et al*.

Abstract

Nanoparticle-based delivery systems for cancer immunotherapies aim to improve the safety and efficacy of these treatments through local delivery to specialized antigen-presenting cells (APCs). Multifunctional mesoporous silica nanoparticles (MSNs), with their large surface areas, their tunable particle and pore sizes and their spatially controlled functionalization, represent a safe and versatile carrier system. In this study, we demonstrate the potential of MSNs as a pH-responsive drug carrier system for the anticancer immune-stimulant R848 (resiquimod), a synthetic Toll-like receptor 7 and 8 agonist. Equipped with a biotin-avidin-cap, the tailor-made nanoparticles showed efficient stimuli-responsive release of their R848 cargo in an environmental pH of 5.5 or below. We showed that the MSNs loaded with R848 were rapidly taken up by APCs into the acidic environment of the lysosome and that they potently activated the immune cells. Upon subcutaneous injection into mice, the particles accumulated in migratory dendritic cells (DCs) in the draining lymph nodes, where they strongly enhanced the activation of the DCs. [...]

Reference

WAGNER, Julia, *et al*. Mesoporous Silica Nanoparticles as pH-Responsive Carrier for the Immune-Activating Drug Resiquimod Enhance the Local Immune Response in Mice. *ACS Nano*, 2021

PMID : 33648336
DOI : 10.1021/acsnano.0c08384

ACSNANO

www.acsnano.org

ARTICLE

Mesoporous Silica Nanoparticles as pH-Responsive Carrier for the Immune-Activating Drug Resiquimod Enhance the Local Immune Response in Mice

Julia Wagner,[⊗] Dorothée Gößl,[⊗] Natasha Ustyanovska, Mengyao Xiong, Daniel Hauser, Olga Zhuzhgova, Sandra Hočevar, Betül Taskoparan, Laura Poller, Stefan Datz, Hanna Engelke, Youssef Daali, Thomas Bein,[*,⊗] and Carole Bourquin[*,⊗]

Cite This: https://dx.doi.org/10.1021/acsnano.0c08384

Read Online

ACCESS | Metrics & More | Article Recommendations | Supporting Information

ABSTRACT: Nanoparticle-based delivery systems for cancer immunotherapies aim to improve the safety and efficacy of these treatments through local delivery to specialized antigen-presenting cells (APCs). Multifunctional mesoporous silica nanoparticles (MSNs), with their large surface areas, their tunable particle and pore sizes, and their spatially controlled functionalization, represent a safe and versatile carrier system. In this study, we demonstrate the potential of MSNs as a pH-responsive drug carrier system for the anticancer immune-stimulant R848 (resiquimod), a synthetic Toll-like receptor 7 and 8 agonist. Equipped with a biotin−avidin cap, the tailor-made nanoparticles showed efficient stimuli-responsive release of their R848 cargo in an environmental pH of 5.5 or below. We showed that the MSNs loaded with R848 were rapidly taken up by APCs into the acidic environment of the lysosome and that they potently activated the immune cells. Upon subcutaneous injection into mice, the particles accumulated in migratory dendritic cells (DCs) in the draining lymph nodes, where they strongly enhanced the activation of the DCs. Furthermore, simultaneous delivery of the model antigen OVA and the adjuvant R848 by MSNs resulted in an augmented antigen-specific T-cell response. The MSNs significantly improved the pharmacokinetic profile of R848 in mice, as the half-life of the drug was increased 6-fold, and at the same time, the systemic exposure was reduced. In summary, we demonstrate that MSNs represent a promising tool for targeted delivery of the immune modulator R848 to APCs and hold considerable potential as a carrier for cancer vaccines.

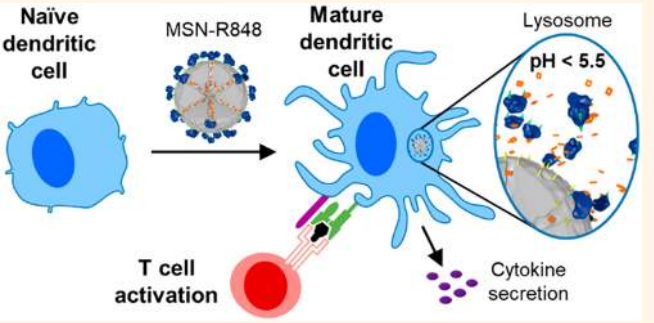

KEYWORDS: *mesoporous silica nanoparticles, drug delivery, immunotherapy, stimuli-responsive capping system, Toll-like receptor 7 agonist, dendritic cell activation, nanovaccine*

In recent years, immunotherapy has revolutionized the field of cancer research by harnessing the power of the immune system to fight cancer.[1] The initiation of a successful anticancer immune response occurs when antigen-presenting cells (APCs) such as dendritic cells (DCs) become activated, undergo maturation, and instruct cytotoxic T cells to kill the cancer cells.[2] However, cancer cells can evade their immune destruction by controlling and suppressing immune cells. One therapeutic strategy to overcome this suppression is therefore to boost the maturation of APCs by pharmacological activation of their Toll-like receptors (TLRs). Several TLR agonists are currently under investigation for use in cancer immunotherapy,[3] and the TLR-7/8 agonist imiquimod has been used successfully for the topical treatment of basal cell carcinoma since 2004.[4] Resiquimod, also called R848, shares a similar structure with imiquimod but was shown to be 100 times more potent.[5,6]

Despite their success for topical treatments, the systemic application of TLR7/8 agonists such as R848 remains clinically

Received: October 6, 2020
Accepted: January 25, 2021

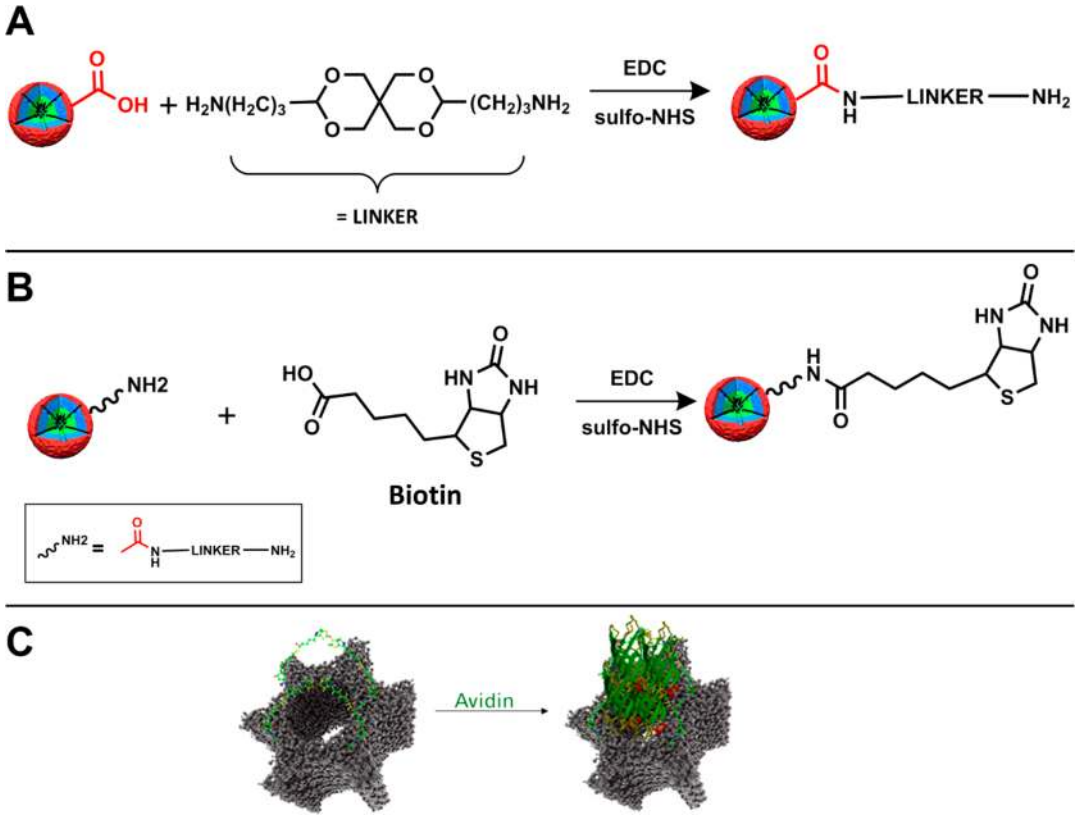

Figure 1. Synthesis schemes of different functionalization steps to construct avidin-capped MSNs. Particle represents co-condensed core−shell MSNs. Green core: phenyl functionality. Blue intermediate layer: pure TEOS. Red external surface: carboxylic moieties. (A) EDC coupling reaction of acetal linker to carboxylic functionalized MSNs. (B) Covalent attachment of biotin to residual amine groups of acetal linker *via* EDC-assisted amidation reaction. (C) Avidin (green) capping of pores (gray) *via* formation of strong avidin−biotin complex. Scheme reprinted with permission from ref 36. Copyright 2009 John Wiley & Sons.

problematic due to their toxicity at the dose required for them to be effective.[7−9] A major challenge with these small molecule immune-activating drugs is their rapid distribution and quick clearance from the body before they reach their target. Better delivery systems are therefore urgently needed to achieve a more localized and sustained immune response in order to enhance the safety and efficacy of these immune-activating drugs. Efficient delivery of R848 to APCs requires a system which (1) ensures that the drug will not be rapidly distributed and eliminated from the body; (2) enables targeted delivery of R848 to APCs and specifically to the endosome, where TLR7/8, the receptors for R848, are located; and (3) limits drug release to the inside of immune cells.

In the search for delivery systems that meet these requirements, the use of nanoparticles has shown great promise. By using DC-targeted nanoparticles that carry immune-activating drugs, several studies were able to demonstrate an increase in cytotoxic T cells in the tumor microenvironment as well as subsequent tumor shrinkage.[10−13] Several of these studies used nanoparticles as a platform for cancer vaccination, meaning that they delivered not only an immune activator such as TLR7/8 ligands to the cells but also a tumor-specific antigen. The most promising nanoparticulate delivery platforms to date include liposomes, polymers, gold nanoparticles (AuNPs), and mesoporous silica nanoparticles (MSNs). Liposomes represent a well-characterized delivery system with several FDA-approved formulations for chemotherapeutic delivery. They are also well-studied for cancer vaccination.[14,15] However, liposomal formulations show a poor control of drug release kinetics. This may lead to either a burst release, often prior to reaching the target, or an impaired release, depending on the hydrophobicity or hydrophilicity of the drug.[16] Other intensively studied materials are poly(D,L-lactic-*co*-glycolic acid) (PLGA) nanoparticles.[17−20] For example, Ilyinskii *et al.* showed that polymeric PLGA nanoparticles loaded with R848 and the antigen OVA could induce a strong and prolonged local immune activation.[21] Although PLGA systems are FDA-approved, it is known that their biodegradation leads to acidic products, such as glycolic and lactic acid, which may degrade the loaded peptides and proteins and may thus limit their delivery. This limitation is amplified by the fact that the polymeric particles can only accommodate hydrophobic or lipophilic drugs, whereas many potent antigens and adjuvants are hydrophilic.[16] In addition, the clinical efficacy of these particles was poor, probably due to the formation of a protein corona *in vivo*, which decreased colloidal stability of the particles and accelerated their clearance by macrophages.[22]

In addition to these organic platforms, metallic platforms such as AuNPs are also being investigated for use in cancer immunotherapy. AuNPs exhibit a versatile surface chemistry and a high affinity toward APCs.[23] In a previous study, we showed that small functionalized gold nanoparticles could successfully load the TLR7/8 ligand R848 in their ligand shell, and we observed enhanced antitumor efficacy with the loaded particles compared to the free drug.[24] Despite those encouraging results, the clinical application of gold nanoparticles is hampered by their high affinity to nucleic acids and related toxicity

https://dx.doi.org/10.1021/acsnano.0c08384
ACS Nano XXXX, XXX, XXX−XXX

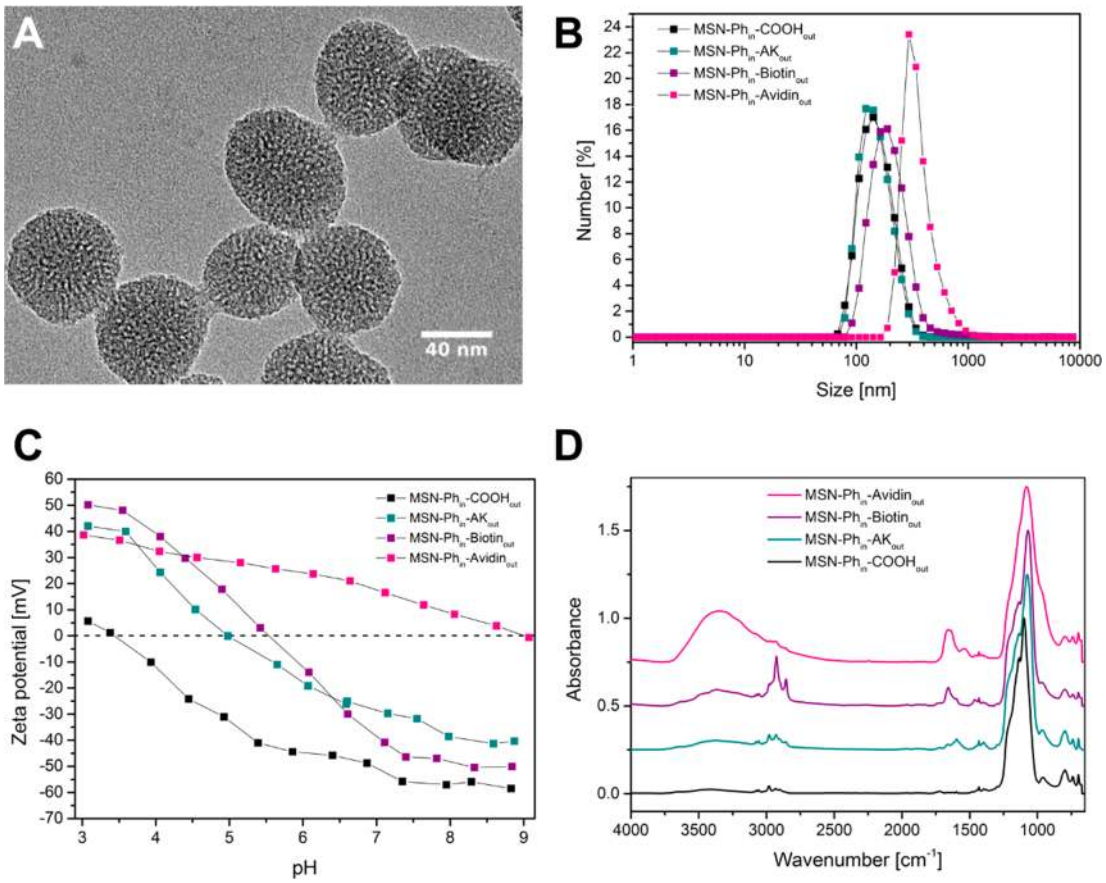

Figure 2. Characterization of functionalized MSNs. (A) TEM image of core−shell MSN−Ph$_{in}$−COOH$_{out}$. (B) DLS measurements of samples MSN−Ph$_{in}$−COOH$_{out}$ (black), MSN−Ph$_{in}$−AK$_{out}$ (cyan), MSN−Ph$_{in}$−biotin$_{out}$ (purple), and MSN−Ph$_{in}$−avidin$_{out}$ (pink). (C) Titration curves of zeta-potential measurements of all four samples. (D) IR spectra of all four samples (for clarity, spectra are shifted by 0.25 units each).

issues.[25,26] The long-term accumulation of AuNPs in the body also raises additional safety concerns.[27]

In view of these limitations of organic and metallic platforms, MSNs represent a promising inorganic drug delivery system. Their size and pore structure can be easily tuned, yielding colloidally stable particles with narrow pore size distributions.[28] Moreover, they possess very large surface areas and pore volumes and thus show high cargo loading efficiencies. They can be functionalized with spatial control, thus enabling perfectly tailored host−guest relations inside the pores as well as a matching external surface allowing for optimized particle−cell interactions.[28,29] With respect to the above-mentioned safety concerns, MSNs show a tunable degradation behavior, resulting in weak silicic acid and related molecules.[30−33] Furthermore, we were able to show in a previous study that these MSNs hold promise as an ideal drug vehicle for immune modulatory cargo.[34]

In this paper, we present spatially segregated core−shell MSNs as a pH-responsive drug carrier system for the immune-stimulant R848. This approach meets all main requirements on a delivery system of R848 to APCs: (1) the encapsulation of R848 ensures that the drug will not be rapidly distributed and eliminated from the body; (2) since the nanoparticles are likely to be taken up by phagocytic cells from the immune system, this can be used as an indirect targeting approach which delivers R848 to phagocytic DCs and specifically to the endosome, where the receptors of R848 are located; and (3) the pH-responsive capping system limits drug release to the inside of phagocytic cells—as the endosome fuses with the lysosome inside the cell, the pH drops and R848 is efficiently released. We thus show that MSNs loaded with R848 are successfully delivered to APCs and produce potent APC maturation *in vitro* and *in vivo*. In addition, we show that adding the antigen OVA to the R848-loaded particles results in augmented T-cell activation. This suggests that MSNs hold strong potential as cancer vaccine carriers.

RESULTS AND DISCUSSION

Synthesis and Characterization of Avidin-Capped MSNs. Core−shell functionalized MSNs were prepared *via* a modified site-specific co-condensation approach with cetyltrimethylammonium chloride (CTAC) as the organic template and tetraethylorthosilicate as the primary silica source.[35]

The core of the particles was functionalized with phenyl groups to accommodate hydrophobic R848, and the external surface was functionalized with carboxylic groups, allowing successive modifications to attach a stimuli-dependent capping system, consisting of a pH-responsive acetal linker and a biotin−avidin complex as the bulky gatekeeper. We previously demonstrated pH-dependent drug release from MSNs using CA (carbonic anhydrase) or PVP (poly(2-vinylpyridine)) as capping systems.[34,37] For the present work, the biotin−avidin cap was chosen because (1) the avidin−biotin interaction is the strongest known noncovalent link between a protein, and its ligand with a dissociation constant of $K_d = 10^{-15}$ M and thus promised to be a robust and tight seal, and (2) biotin and avidin

https://dx.doi.org/10.1021/acsnano.0c08384
ACS Nano XXXX, XXX, XXX−XXX

are both naturally occurring biomolecules that are considered low to nonimmunogenic.[38,39]

In the first step of subsequent core−shell MSN modification, shown in Figure 1A, the pH-responsive acetal linker (AK; 3,9-bis(3-aminopropyl)-2,4,8,10-tetraoxaspiro[5.5]undecane) was covalently bound to the carboxylic-functionalized periphery of the particles *via* an EDC (*N*-(3-(dimethylamino)propyl)-*N*-ethylcarbodiimide hydrochloride)-assisted amidation reaction. This step was followed by a second EDC coupling between the residual amine group of the attached acetal linker and the COOH group of biotin (Figure 1B). Capping of the pores was achieved through noncovalent attachment of avidin through formation of the biotin−avidin complex. Avidin possesses four binding sites for biotin. It was therefore added in great excess to avoid any cross-coupling reaction between two or more different particles. With its dimensions of 5 × 5 × 4 nm^3, avidin is big enough to completely block the 3.2 nm pores.[40] The concept is shown in Figure 1C.[36]

The transmission electron microscope (TEM) image of the template-free core−shell MSNs showed spherical particles with sizes of around 70 nm and a wormlike pore structure (Figure 2A). Dynamic light scattering (DLS) measurements revealed colloidally stable particles with a narrow particle size distribution (Figure 2B). Particle sizes obtained with this method showed a mean value of 146 nm (hydrodynamic diameter) for the core−shell MSN−Ph_{in}−$COOH_{out}$. Functionalization with an acetal linker and biotin showed only a moderate increase in effective size up to a mean value of 183 nm. DLS measurements of avidin-capped particles in aqueous solutions demonstrated a shift to higher effective sizes of around 280 nm. This can be explained by the attachment of the bulky protein (66−67 kDa) as well as a small agglomeration effect.[41] The difference in the sizes measured by TEM and DLS can be partially attributed to the larger hydrodynamic radius of the particles measured in solution and determined with DLS. Some additional agglomeration effect may also contribute to the increased size measured with DLS. Additionally, a study by Cauda *et al.* showed that DLS leads to a systematic overestimation of size compared to techniques like TEM, scanning electron microscopy, and fluorescence correlation spectroscopy.[42]

Zeta-potential measurements were used to monitor the different functionalization steps (Figure 2C and Table 1). MSN−Ph_{in}−$COOH_{out}$ showed an isoelectric point (IEP) of 3.4 and a zeta-potential of almost −50 mV. This negative zeta-potential confirmed the successful implementation of TEPSA (3-(triethoxysilyl)propylsuccinic anhydride), including the ring opening of the succinic anhydride of the organosilane and the resulting two adjacent carboxyl groups. After attachment of the acetal linker, the IEP is shifted to higher pH values by almost 1.5 because of the residual amine end groups of the linker, which are positively charged at acidic pH. MSN−Ph_{in}−$biotin_{out}$ possessed an IEP of pH 5.5, which can be explained by the urea-containing motif in biotin. Through the possible resonance forms, at least one of the two nitrogen atoms is protonated at slightly acidic pH. Adding avidin to the particles resulted in a zeta-potential of around +20 mV and a large shift of the isoelectric point to a pH value of 9.01, which is due to the large number of N-termini present in the protein cap.

The different surface functionalization steps, including the capping with avidin, were also apparent in IR spectra, as shown in Figure 2D. The silica framework vibrations were visible in all spectra in the region between 1240 and 1000 cm^{-1}. Furthermore, the phenyl core of the MSNs was indicated in

Table 1. Summary of N_2 Sorption Measurements and Isoelectric Points of Corresponding Zeta-Potential Measurements

Sample	Surface Area [m^2/g]	Pore Volume [cm^3/g]	Pore Size [nm]	IEP
MSN-Ph_{in}-$COOH_{out}$	1006	0.92	3.2	3.44
MSN-Ph_{in}-AK_{out}	824	0.73	3.2	4.98
MSN-Ph_{in}-$Biotin_{out}$	1025	0.79	3.2	5.53
MSN-Ph_{in}-$Avidin_{out}$	32	-	-	9.01

all samples by a peak at 1431 cm^{-1} (C═C stretching vibrations) and modes at 3077 and 3059 cm^{-1} due to the aromatic C−H stretching vibrations of the phenyl ring. Sample MSN−Ph_{in}−$COOH_{out}$ showed additional peaks at 1740 and 1720 cm^{-1} belonging to the COOH stretching vibrations of saturated dicarboxylic acids. This proved the successful *in situ* ring opening of the succinic anhydride silane TEPSA. Addition of the acetal linker *via* amidation reaction resulted in a new vibration band at 1599 cm^{-1}, which can be attributed to the deformation vibration of free amines, present at the unbound site of the homobifunctional linker. After biotinylation *via* EDC amidation, a new C═O stretching vibration arises at 1658 cm^{-1} belonging to the biotin group. This peak was obscured upon avidin addition by the amide I and II stretching vibrations, occurring at 1660 cm^{-1} (amide I: C═O stretching vibration) and 1640 cm^{-1} (amide II: N−H deformation and C−N stretching vibration).

Thermogravimetric analysis (TGA) proved the incorporation of a large phenyl content with an observable mass loss of 28% in the sample MSN−Ph_{in}−$COOH_{out}$ (supplemental Figure S1A,B). Additionally, we confirmed successful functionalization by monitoring the presence of free amine groups in a fluram assay (supplemental Figure S1C).

All samples except MSN−Ph_{in}-$avidin_{out}$ exhibited a type IV nitrogen sorption isotherm and a large specific surface area, which is typical for mesoporous materials. The avidin-capped sample showed a type II isotherm which is attributable to nonporous materials and proved the successful pore closure mechanism (Figure 3A). The Brunauer−Emmett−Teller (BET) surface areas were calculated from the respective isotherms in the range of p/p_0 = 0.05−0.2. The mean pore size of MSN−Ph_{in}−$COOH_{out}$ was calculated to be 3.2 nm. This is smaller than that for most other MSN nanoparticles, which show pore sizes of around 4 nm. The reduction in pore size can be attributed to the successful incorporation of a large phenyl content in the MSNs. It has been reported that, in contrast to hydrophilic organic moieties, hydrophobic organosilanes are capable of aligning with the hydrophobic tails of the amphiphilic templates instead of disturbing the micelle structure.[43] This results in smaller particle sizes and shows a pore shrinking effect in comparison to incorporation of other organosilanes (which would commonly lead to 4 nm pores).[35,44,45] Modifications of the particle's external surface with an acetal linker and biotin

https://dx.doi.org/10.1021/acsnano.0c08384
ACS Nano XXXX, XXX, XXX−XXX

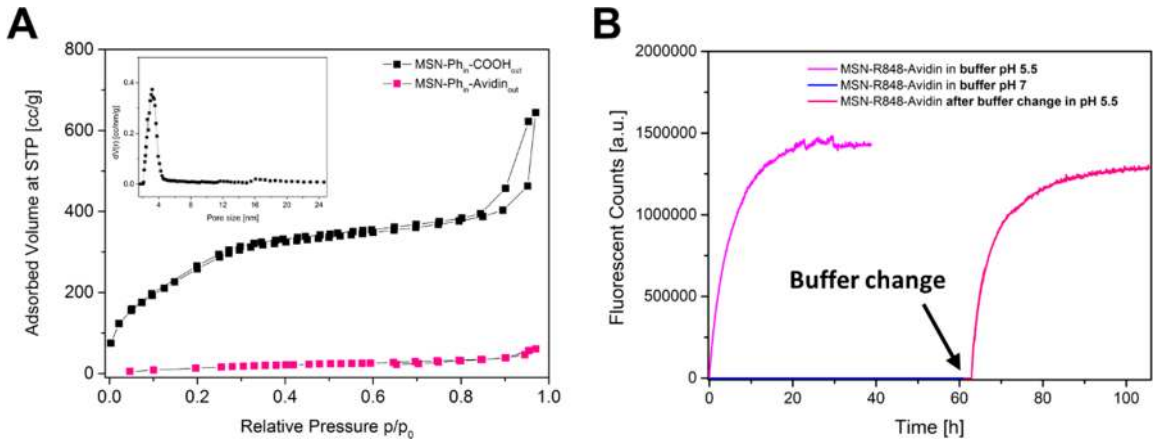

Figure 3. Capping system closes pores tightly at physiological pH and efficiently opens up at low pH. (A) BET isotherm and pore size distribution (inset) for clarity reasons only shown for sample MSN−Ph_{in}−$COOH_{out}$ (black) and MSN−Ph_{in}-$avidin_{out}$ (pink). (B) Buffer change experiment proves long-term stability of MSN−R848-avidin at physiological pH. Time-based fluorescent release of resiquimod was measured simultaneously at pH 5.5 (MES buffer, pink curve) and pH 7.0 (SSC buffer, blue curve) at 37 °C. After 60 h, the cap containing tightly closed MSNs at pH 7.0 was moved to a cuvette filled with fresh MES buffer (pH 5.5), and the release was measured for another 60 h.

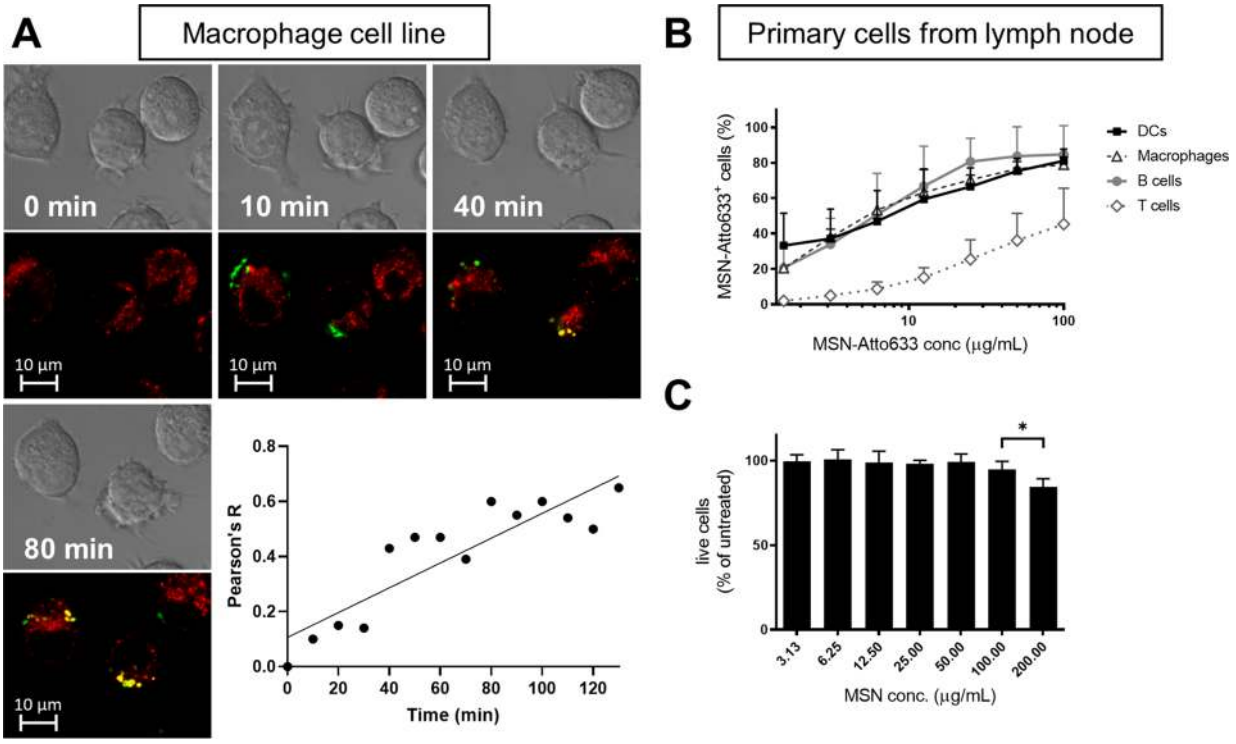

Figure 4. MSNs are taken up into the lysosome of APCs. (A) J774A.1 macrophages were stained with the lysosomal marker LysoTracker (red) before adding Atto633-labeled MSNs (green) to the cells at time point 0 min. Images of live cells were taken every 10 min. The colocalization analysis Pearson's *R* was performed for each frame. (B,C) Mouse lymph node cells were incubated with increasing concentrations of MSN−Atto633 for 24 h and analyzed by flow cytometry. The association of MSN−Atto633 (B) was analyzed in different cell populations: DCs ($CD19^-CD3^-CD11c^+$), macrophages ($CD19^-CD3^-CD11b^+$), B cells ($CD19^+CD3^-$), and T cells ($CD19^-CD3^+$). Live cells were determined by flow cytometry (C). The graphs show the mean and standard deviation of a minimum of four independent experiments. For statistical analysis, one-way ANOVA was used.

have no significant impact on the pore size. This illustrates the spatial control over the selective functionalization of the external surface with little or no effect on the pore accessibility. All results from nitrogen sorption measurements are summarized in Table 1.

The phenyl core of the MSNs facilitates loading of the hydrophobic drug R848. Without phenyl groups, R848 cannot be loaded into the MSNs. This is demonstrated by an exchange of phenyl groups with amine groups, which almost completely prevented loading of the drug due to electrostatic repulsion (Figure S2). This underlines the pronounced effect of the particles' interior pore wall decoration on drug loading efficiency. To optimize the process further, the most efficient loading buffer was identified. To enable hydrophobic interaction between R848 and the phenyl moieties inside the pores, a buffer with antichaotropic or rather kosmotropic ions was chosen

https://dx.doi.org/10.1021/acsnano.0c08384
ACS Nano XXXX, XXX, XXX−XXX

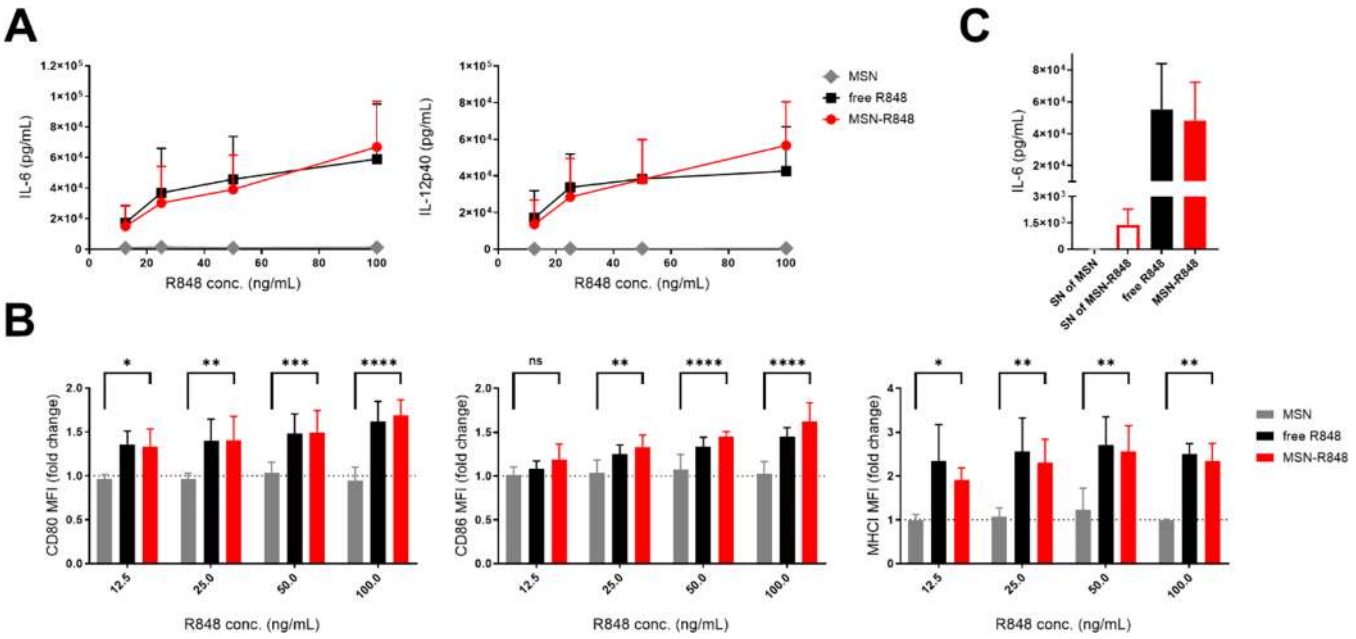

Figure 5. R848-loaded MSNs successfully activate DCs. BMDCs were incubated with increasing concentrations of MSN−R848. The amount of MSN−R848 was adjusted to reach an equimolar amount between loaded or free R848. (A) Secretion of the cytokines IL-6 and IL-12p40 was measured in the cell culture supernatants by ELISA. (B) Cell surface expression of the MHC I complex and of the co-stimulatory molecules CD80 and CD86 was assessed by flow cytometry. The mean fluorescence intensity (MFI) in live cells is expressed relative to the unstimulated control. (C) BMDCs were incubated with supernatants (SN) from different MSN−R848 batches for 24 h. The volume of SN transferred to the cells was equalized to the volume used for the MSN−R848 control condition. As positive controls, 50 ng/mL of free or MSN-loaded R848 was added to the BMDCs. IL-6 production was measured in the cell culture supernatants by ELISA. The graphs show the mean and standard deviation of a minimum of four independent experiments. For statistical analysis, the two-way ANOVA was used.

according to the Hofmeister series.[46−51] As can be seen in supplemental Figure S2, SSC20x buffer led to the best loading result of the phenyl-functionalized MSNs.

To ensure that the successful pore closing—shown with sorption measurements in Figure 3A—also worked with MSN−R848 loaded in SSC20x, an in cuvette release experiment was performed. We carried out a time-based release study in two different buffers at pH 7.0 and pH 5.5. The release of the hydrophobic R848 from the MSNs in the acidic environment occurs most likely due to protonation of aromatic amines present in the molecule, which creates a net positive charge and renders the molecule water-soluble. The amount of released R848 was calculated with the help of calibration curves in the respective buffers, taking the difference in pH-dependent fluorescence of R848 into account (supplemental Figure S3). We measured both samples in parallel with a multicuvette holder at 37 °C for 60 h. To prove that the sample at pH 7.0 (blue curve Figure 3B) was tightly sealed and did not lose its ability to open up at lower pH, we performed a buffer change experiment. To this end, after measuring for 60 h at 37 °C at pH 7.0, the membrane-sealed cap with R848-loaded MSNs redispersed in SSC20x buffer was transferred to a cuvette with fresh MES buffer (pH 5.5), which simulates the pH of the lysosome and triggers opening of the capping system. After 2−3 h, the SSC20x buffer in the cap was completely exchanged with MES buffer. The resulting hydrolysis of the acetal linker induced increasing amounts of detected R848 (dark pink curve). Thus, the MSN−R848 system demonstrated long-term stability and efficient pH-responsive R848 release.

All in all, we could show that multifunctional core−shell MSNs were successfully modified with a pH-responsive acetal linker, followed by biotinylation, which enabled the closing of the pores *via* the formation of a strong biotin−avidin complex as well as their reopening upon acidification of the surrounding media.

MSNs Are Taken up into the Endolysosomes of Antigen-Presenting Cells. For successful delivery of R848 by the avidin-capped MSNs, it is important that the particles are efficiently taken up by APCs and that they accumulate in the acidic environment of the lysosome to ensure targeted drug release. To examine whether the MSNs were taken up by immune cells, fluorescently labeled MSNs were added to a macrophage cell line and analyzed by live cell imaging. Association of MSNs with the cells was already visible 10 min after addition of the nanoparticles (green) to the culture. After 40 min, a clear colocalization was apparent between the lysosomes (red) and the MSNs (colocalization: yellow) (Figure 4A and supplemental video). Additionally, the colocalization analysis Pearson's *R* was performed for every frame. Since the MSNs were added at time point 0, there is no overlap. However, Pearson's *R* increased over the course of the data collection, which indicates MSN uptake into the lysosomes.

In order to examine the association of MSNs with different types of primary immune cells, freshly isolated murine lymph node cells and splenocytes were incubated with increasing concentrations of fluorescently labeled MSNs. As shown in Figure 4B (and supplemental Figure S4A), the proportion of MSN-positive DCs, macrophages, and B cells increased in a concentration-dependent manner. This association was so efficient that, at higher MSN concentrations, 80% of all DCs, macrophages, and B cells were MSN-positive. As macrophages and dendritic cells are potent phagocytic cells, it is probable that nanoparticles are at least partly taken up by these cells, as was the case with the macrophage cell line in Figure 4A. Indeed, MSN

https://dx.doi.org/10.1021/acsnano.0c08384
ACS Nano XXXX, XXX, XXX−XXX

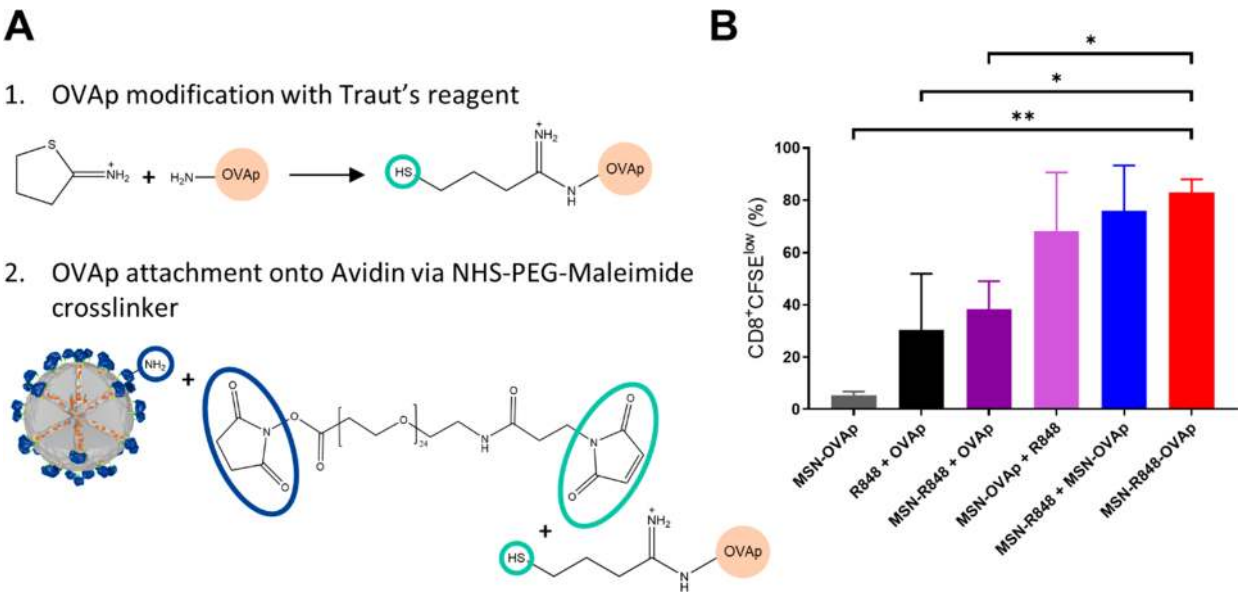

Figure 6. MSN−R848−OVAp particles induce T-cell proliferation *in vitro*. (A) Covalent attachment of OVAp to MSNs. OVAp, thiolated with Traut's reagent (1), was coupled to MSNs' avidin cap through a heterobifunctional maleimide-PEG-NHS cross-linker (2). (B) BMDCs were exposed to different combinations of R848- and/or OVA peptide (=SIINFEKL)-loaded MSN. The amount of MSN−R848 was adjusted to reach the equimolar amount of 50 ng/mL R848 between loaded or free R848; free OVA peptide was used at a concentration of 10 ng/mL. After 24 h, OVA-specific, CFSE-labeled $CD8^+$ T cells were added to the BMDCs and cocultured for another 2−3 days. Proliferation of T cells was determined by analysis of CFSE content ($CFSE^{low}$) with flow cytometry. The graph shows the mean and standard deviation of three independent experiments. For statistical analysis, one-way ANOVA was performed.

uptake into cells has already been demonstrated for primary splenocytes, primary macrophages, and other macrophage cell lines.[34,52,53] T lymphocytes, on the other hand, were only MSN-positive at higher concentrations. Since T lymphocytes are not professional antigen-presenting cells, this phenotype might rather be due to an attachment of the particles to the cell surface.[54]

To examine whether MSNs were toxic to primary immune cells, freshly isolated murine lymph node cells were incubated with increasing concentrations of MSNs and their viability was assessed. No decrease in the viability of lymph node cells was observed at MSN concentrations up to 100 μg/mL after 24 h (Figure 4C and supplemental Figure S4B), and this was also true for the macrophage cell line and bone-marrow-derived dendritic cells (BMDCs) (supplemental Figure S4C,D).

In summary, the MSNs did not show immunotoxicity up to 100 μg/mL and were readily taken up by APCs.[34] Therefore, this system fulfills essential requirements for a promising pH-responsive delivery vehicle for immune-activating drugs.

R848-Loaded MSNs Successfully Activate Dendritic Cells in Culture. DCs are among the most potent APCs. Upon encounter with pathogens or other "danger" signals, DCs mature and become activated. This results in the expression of high levels of MHC and co-stimulatory molecules on their surface as well as the secretion of pro-inflammatory cytokines, all of which are prerequisites for a successful induction of immune responses.[55] Immune-activating drugs such as resiquimod (R848) can act on DCs to stimulate them in a similar manner.

To evaluate the release efficiency of the biotin−avidin system in a functional manner, we investigated the impact of R848-loaded MSNs on the activation of DCs. To this end, we incubated BMDCs with different concentrations of R848-loaded MSNs or with a corresponding amount of free R848 or unloaded MSNs. MSN−R848 induced secretion of high amounts of the pro-inflammatory cytokines IL-6 and IL-12p40 (Figure 5A) and led to upregulation of the co-stimulatory molecules CD80 and CD86 and of the MHC I complex, which was similar to the effect of free R848 (Figure 5B). The unloaded MSNs did not show any immune-activating properties.

To further investigate the impact of the lysosomal pH drop on the functionality of MSN−R848, BMDCs were incubated in the presence of the endolysosomal acidification inhibitor chloroquine. Chloroquine is a diprotic weak base and can diffuse freely into endosomes, lysosomes, and Golgi vesicles, where it accumulates, becomes protonated, and thus increases the local pH.[56] As seen in supplemental Figure S5, chloroquine indeed prevented IL-6 production and up-regulation of CD86 in BMDCs cultured with MSN−R848. This demonstrates that the endolysosomal pH drop was crucial for the immune-activating function of MSN−R848.

Additionally, we tested the release of R848 by MSNs in different cell culture media using a functional assay. The supernatants from MSN−R848 incubated overnight in cell-free phosphate-buffered saline (PBS) at 4 °C induced only very low levels of IL-6 production in BMDCs (Figure 5C and supplemental Figure S6). Supernatants from MSN−R848 incubated at 37 °C for 24 h in cell-free PBS, cell culture medium, or fetal bovine serum (FBS) induced slightly higher levels of IL-6 production by BMDCs. However, these were still low compared to the levels induced by the same amount of free R848 or R848-loaded MSNs applied directly to the cells (supplemental Figure S6). The data indicate that R848-loaded MSNs released only small amounts of the drug when suspended in cell culture media.

In conclusion, we have developed a system that can efficiently deliver the immune-stimulant R848 to APCs and induce a robust immune response.

MSN−R848 Particles Coloaded with Antigen Enhance T-Cell Proliferation. Activation of cytotoxic $CD8^+$ T cells, followed by their proliferation, occurs when they recognize a

https://dx.doi.org/10.1021/acsnano.0c08384
ACS Nano XXXX, XXX, XXX−XXX

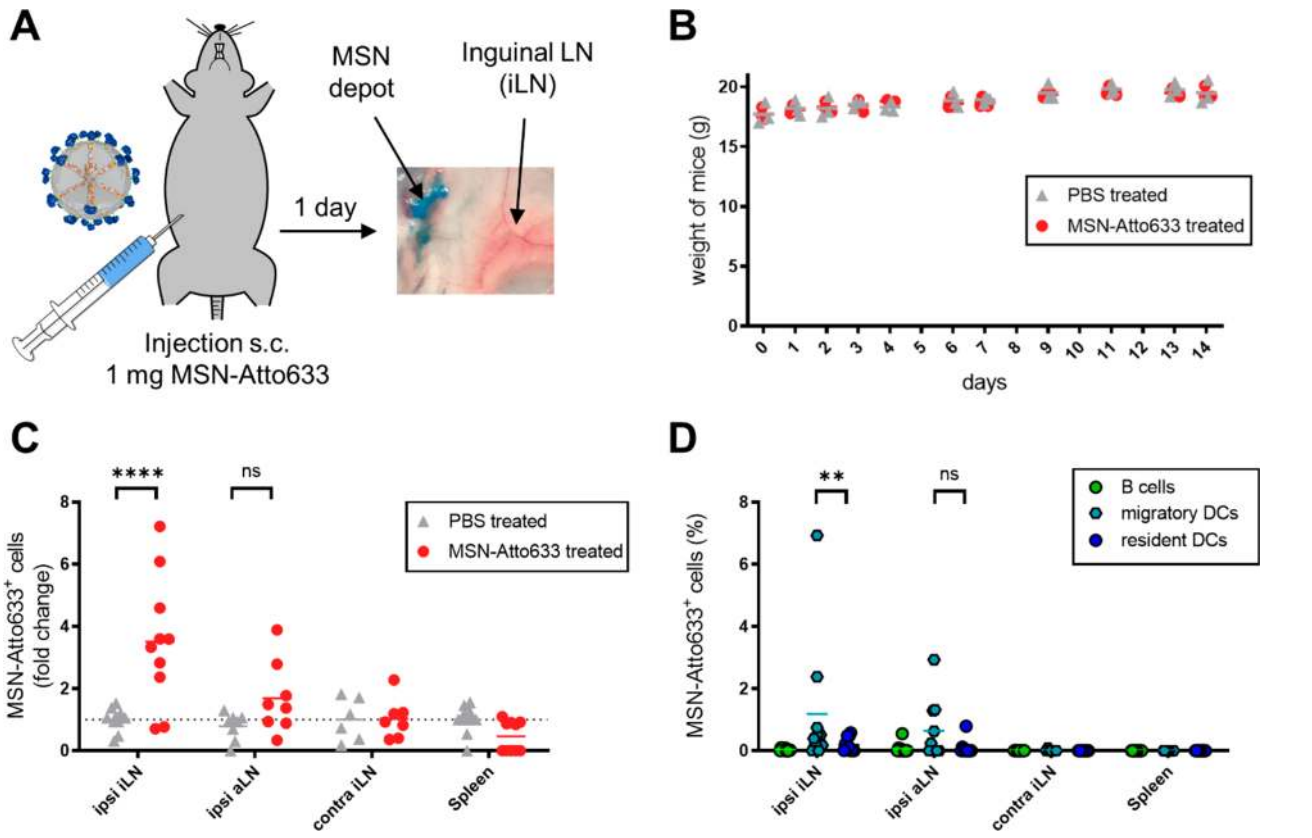

Figure 7. MSNs are not toxic *in vivo* and are mainly found in the draining lymph nodes in migratory DCs. (A) Amounts of 1 mg of Atto633-labeled MSNs were subcutaneously injected into the right hind limb of mice. (B) Weight of the mice was measured at indicated time points over a period of 14 days. (C) Ipsilateral and contralateral lymph nodes and spleens were analyzed after 24 h by flow cytometry. The amount of MSN−Atto633$^+$ cells in the different organs was compared to the control group (PBS). (D) Uptake of MSN−Atto633 was analyzed in different cell populations: B cells ($CD45^+CD3^-CD19^+$), resident DCs ($CD45^+CD3^-CD19^-CD11c^+MHCII^{low}$), migratory DCs ($CD45^+CD3^-CD19^-CD11c^+MHCII^{high}$). Every point on the graphs represents one mouse, and the mean is shown for n = 3−10. For statistical analysis, the two-way ANOVA was used.

specific antigen presented by activated and matured APCs. Cancer vaccines take advantage of this phenomenon by associating a tumor-specific antigen with an immune-activating adjuvant to induce a strong T-cell response against the tumor.[57] In order to enhance the MSN−R848 delivery system and induce an antigen-specific immune response, a well-characterized immunodominant peptide derived from the model antigen ovalbumin (OVAp) was attached to the outer surface of the MSNs. For this, the OVAp was thiolated with Traut's reagent and then covalently attached to the avidin cap *via* a bifunctional PEG cross-linker (Figure 6A).

To examine whether MSNs coloaded with R848 and OVAp peptide antigen (MSN−R848−OVAp) led to dendritic cell activation, BMDCs were incubated with increasing concentrations of loaded MSNs. MSN−R848−OVAp induced the production of IL-6 by BMDCs in a dose-dependent manner but at levels lower than those of MSN−R848 (supplemental Figure S7A). To investigate the potential of MSN−R848−OVAp to induce activation and proliferation of T cells, OVAp-specific mouse T cells were cocultured with BMDCs stimulated with R848- and/or OVAp-loaded MSN particles. To measure proliferation, T cells were labeled with the fluorescent dye CFSE. As shown in Figure 6B, over 80% of the T cells had divided at least once ($CD8^+CFSE^{low}$) when incubated with MSN−R848−OVAp-stimulated BMDCs (gating strategy can be found in supplemental Figure S7B). Importantly, this was considerably more than with MSN−R848 plus free OVAp or with free R848 and free OVAp. In conclusion, DCs stimulated with MSNs loaded with both R848 and antigen induced a potent cytotoxic T-cell response and seem promising as vaccine carriers.

Biodistribution of MSNs in Mice. After proving the robust activation of immune cells by pH-responsive MSNs carrying R848 *in vitro*, their safety and biodistribution was investigated *in vivo*. C57BL/6 mice were injected subcutaneously (s.c.) with 1 mg of fluorescent Atto633-labeled MSNs, which formed a depot at the injection site, or PBS (scheme in Figure 7A) and observed daily for 14 days. In this time period, the mice did not show any signs of toxicity and gained weight similarly to the control group (Figure 7B). Furthermore, previous studies have already shown that doses of 1 mg or less MSNs are safe to use in rodents.[58,59]

The initiation of a robust immune response mainly occurs in lymphoid structures such as lymph nodes and the spleen, where matured DCs activate T cells. Thus, bringing nanoparticles carrying immune-stimulating drugs to these sites is of vital importance. To evaluate the biodistribution of the avidin-capped MSNs, lymphoid organs of mice were analyzed 1 day after MSN−Atto633 injection. The ipsilateral inguinal and axillary as well as the contralateral inguinal lymph nodes and the spleen were investigated for MSN−Atto633$^+$ cells by flow cytometry (classification of LNs in supplemental Figure S8). We found the highest amount of MSN$^+$ cells in the ipsilateral inguinal lymph node (iLN), which is the main draining lymph node for the injection site (Figure 7C). Some mice also showed

https://dx.doi.org/10.1021/acsnano.0c08384
ACS Nano XXXX, XXX, XXX−XXX

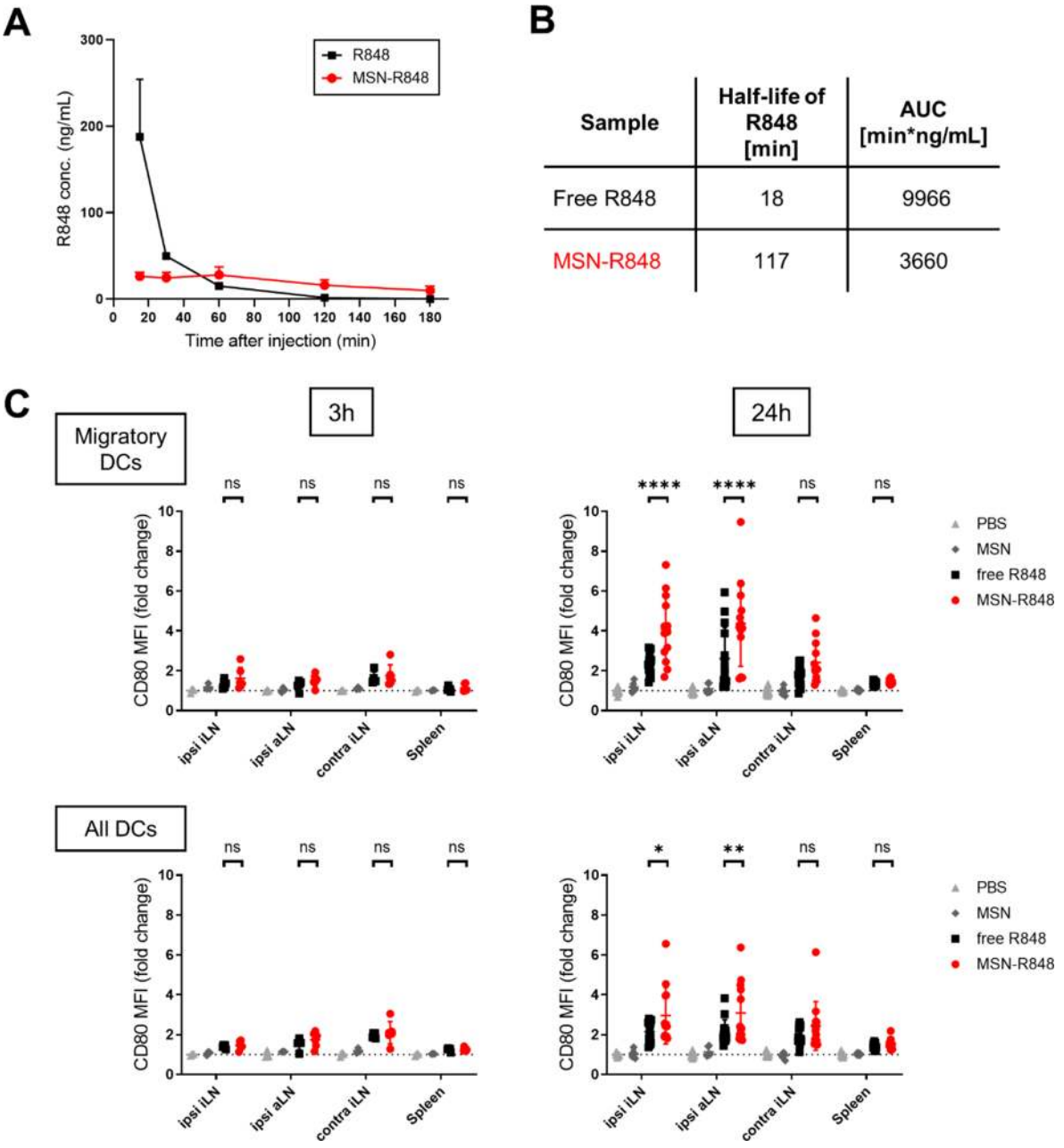

Figure 8. Kinetics of R848 distribution in serum and DC activation in lymphoid organs. Mice were injected subcutaneously into the right hind limb with MSN−R848, free R848 (10 μg), unloaded MSNs or PBS. The amount of MSN−R848 to be injected was calculated with the help of R848 release measurements and adjusted to reach 10 μg of R848 per mouse. (A) R848 distribution was measured in mouse serum by LC-MS/MS at 15, 30, 60, 120, and 180 min after injection. The graph shows the mean and standard deviation of n = 3−8 mice. (B) Summary of two pharmacokinetic parameters: the half-life of R848 in the serum and the area under the curve for free R848 and MSN−R848 is shown. (C) After 3 or 24 h, the ipsilateral and contralateral lymph nodes and spleens were analyzed by flow cytometry. The upregulation of CD80 mean fluorescence intensity in all DCs ($CD45^+CD19^-CD3^-CD11c^+$) and in the migratory DC population ($CD45^+CD19^-CD3^-CD11c^+CD11b^-CD103^+$) was assessed relative to the PBS control. Every point on the graphs represents one mouse, and the mean and standard deviation are shown for 3 h (n = 3−6) and 24 h (n = 6−13). For statistical analysis, the two-way ANOVA was performed.

MSN^+ cells in the ipsilateral axillary lymph node (aLN), which is a secondary draining lymph node. However, these mice had less MSN^+ cells in the iLN, which suggested that small variations in the injection site could have led to an injection in the area draining the aLN.

In all mice, we consistently found that the contralateral lymph nodes and the spleen did not show any MSN−$Atto633^+$ cells after 24 h. After further analyzing the different cell populations in the ipsilateral lymph nodes, we showed that it were mainly migratory DCs rather than resident DCs that took up the MSNs (Figure 7D). Migratory DCs patrol most of the body's tissues in search for invaders or aberrant cells. If they encounter foreign structures, they become activated and migrate to the next draining lymphoid organ to initiate an immune response. Resident DCs, by contrast, rely on foreign material to be brought or drained directly to the lymphoid organs as they are restricted

https://dx.doi.org/10.1021/acsnano.0c08384
ACS Nano XXXX, XXX, XXX−XXX

to these sites.[60] Here, we could show that MSNs were predominantly taken up by patrolling migratory DCs and carried to the next draining lymph node.

Kinetics of Immune Cell Activation in Mice. R848 is a low molecular weight compound (314.4 Da) and therefore expected to distribute fast and be rapidly cleared from the body upon injection. To compare the pharmacokinetics of free R848 and R848 delivered by MSNs, we measured R848 concentrations in the blood by LC-MS/MS (liquid chromatography−mass spectrometry). For this, C57BL/6 mice were injected s.c. with MSN−R848 or free R848 (at an equimolar amount of 10 μg of R848), and serum was collected at several time points up to 3 h. From previous experiments and literature, we know that 10 μg of R848 is well-tolerated in mice and does not lead to side effects.[61−63] With minor variations of loading efficiencies between different MSN−R848 batches, the injected MSN amount corresponded to 270−370 μg of MSNs per mouse and thus remained well below the 1 mg MSNs injected for the *in vivo* safety experiment. As expected for the serum measurements, the concentration of free R848 was highest at the earliest time point around 200 ng/mL, measured 15 min after injection, and vanished quickly thereafter. At 3 h after injection, R848 was barely measurable in the serum (Figure 8A). On the contrary, R848 concentrations in the serum were much lower with MSN−R848 and stayed well below 40 ng/mL. Importantly, the half-life of R848 in the serum increased from 18 min for free R848 to 117 min for MSN−R848, and the area under the curve (AUC) was about 3-fold higher for free R848 (Figure 8B), meaning that the systemic exposure of mice to R848 was much higher with free R848 than with MSN-delivered R848. Taken together, this reflects a low, steady, and slow release of the drug rather than a burst effect.

To assess the activation of immune cells by R848-loaded MSNs in mice, we analyzed different lymphoid organs of the mice at an early (3 h) and later (24 h) time point after s.c. injection (the gating strategy can be found in supplemental Figure S9). After 3 h, we observed a low activation of DCs and B cells in lymph nodes on the ipsi- and contralateral sides of injection (Figure 8C and supplemental Figure S10, left panels). This early low activation, which is apparent through the upregulation of the co-stimulatory molecules CD80 and CD86, may have been induced by free R848 released from the particles. This finding is consistent with the low serum concentrations of R848 from Figure 8A and is supported by the fact that we also find similar levels of the pro-inflammatory cytokines IL-6, TNFα, and IL-12p40 in the serum 3 h after injection of free R848 and MSN−R848 (supplemental Figure S11).

After 24 h, however, the activation state of DCs and especially the migratory DCs in the draining ipsilateral inguinal and axillary lymph nodes was substantially more pronounced. Importantly, upregulation of CD80 and CD86 on migratory DCs in the draining lymph nodes was significantly stronger in mice injected with the R848-loaded particles compared to free R848 (Figure 8C and supplemental Figure S10, right panels). The proportion of skin-draining migratory DCs are known to reach a plateau in the draining lymph nodes around 24 h after s.c. injection.[64,65] Thus, at this later time point, the activation state of the DCs was considerably enhanced, most likely by newly arrived migratory DCs that took up MSN−R848, became strongly activated, and migrated to the closest lymph nodes, meaning that the enhancement of the immune response was localized to the draining ipsilateral side. This is also consistent with the fact that most MSN^+ migratory DCs were found in the draining lymph nodes.

All in all, R848-loaded MSNs strongly augmented the immune response in the draining lymph nodes after 24 h, in all likelihood by activating the skin-draining migratory DC population that, after uptake of the particles, moved to the ipsilateral lymph nodes.

In this study, we developed a pH-responsive delivery system for the immune-activating drug R848. We demonstrated that correctly tailoring the multifunctional MSNs enabled enhanced loading of the hydrophobic molecule R848. For this purpose, we performed a delayed co-condensation approach, developed in our group, to introduce phenyl groups solely into the pores.[44] It was proven before that this synthesis procedure allows spatial control over incorporated organic moieties.[35] Delayed functionalization of the exterior surface in the same synthesis procedure with carboxylic groups allowed for further modification with a pH-responsive acetal linker and a biotin−avidin capping system. The pH-dependent hydrolysis of the linker enables stimuli-responsive opening of the pores.[66] Once the pH in the endolysosome drops to a value of pH 5.5, the cleavage of the applied acetal linker is triggered, inducing pore opening and drug release through complete detachment of the bulky biotin−avidin complex.[67]

In addition to tightly closing the drug-loaded pores, capping of the MSNs with the protein avidin also leads to improved particle−cell interactions. As shown by van Rijt *et al.*, avidin coating of the MSNs results in enhanced biocompatibility.[68] Compared to amine-functionalized MSNs, which were shown to exhibit a strong protein corona formation, avidin coating of the particles minimizes this effect and the subsequent clearance by macrophages.[69] Furthermore, Zhang *et al.* reported that anionic vaccines were not taken up by APCs due to the repulsion of negatively charged particles and negatively charged phospholipid bilayers of the cell membranes.[70] The dramatic change in surface charge after attachment of avidin to the MSNs, as seen by a shift in zeta-potential from −50 mV ($MSN-Ph_{in}-COOH_{out}$) to +20 mV ($MSN-Ph_{in}-avidin_{out}$), enables an attractive particle−DC interaction and thus facilitates the uptake by APCs. Indeed, successful uptake of avidin-coated MSNs in APCs *in vitro* was already observed within 30 min.

Not just *in vitro* but also *in vivo*, we could show that the MSN delivery system was preferentially taken up by APCs. After subcutaneous injection of the particles into mice, the MSNs were mainly found in migratory DCs in the draining lymph nodes, which are the site of immune response initiation. The size of nanoparticles plays a major role in their distribution in the body. Whereas nanoparticles larger than 50−100 nm tend to remain trapped in the extracellular matrix at the injection site, smaller particles (below 50 nm) drain directly to the lymphatic system or blood.[71] With a particle size of around 280 nm, the avidin-capped MSNs are too large to be drained with the interstitial flow to the lymph nodes and thus create a small depot at the injection site. By taking advantage of patrolling migratory DCs that take up foreign material such as nanoparticles, become activated, migrate to the closest lymph nodes, and initiate the immune response there, a major drawback of smaller particles can be avoided. Smaller particles distribute more quickly in the lymphatics and can also enter the bloodstream, where they are subject to clearance by the liver, kidneys, or spleen.[72] This may lead to unwanted toxic side effects and a much faster turnover of the delivered drug.

https://dx.doi.org/10.1021/acsnano.0c08384
ACS Nano XXXX, XXX, XXX−XXX

Importantly, when loaded with R848, the particles considerably enhanced activation of the skin-draining migratory DCs in the lymph nodes after 1 day. Thus, the MSN-delivered R848 is more effective than free R848, which vanishes from the system quickly. Hydrophobic small molecule drugs that are passively loaded into nanoparticles often exhibit poor release control or even a fast burst release.[16,73] In contrast, our results show that when R848 was encapsulated in pH-responsive, capped MSNs, a burst release was prevented. Moreover, by directly measuring R848 concentrations in the blood, we demonstrated that with MSN−R848, the pharmacokinetic profile was much improved.

Furthermore, we demonstrated that MSNs that simultaneously carried the adjuvant R848 and the model antigen OVA induced potent T-cell activation and proliferation. As previously shown, simultaneous delivery of both adjuvant and antigen to the same cell increases the potency of a vaccine.[74] The importance of this phenomenon is also apparent with the MSN−R848−OVAp particles as the dual delivery of antigen and adjuvant within one particle seems to compensate for the reduced BMDC activation by MSN−R848−OVAp. This underlines the great potential of MSNs as combined carrier system for both adjuvant and antigen. In this work, we used the OVA peptide as a model antigen. However, the system is easily adaptable and other antigens could be attached to avidin *via* its functional groups. This means that even several different tumor-specific antigens could be loaded onto the MSNs to achieve a stronger antitumor effect.[75−80] Furthermore, the MSNs could also accommodate patient-specific tumor antigens to generate a "personalized" MSN vaccine carrier system.[81] The adjustability of the pore size of mesoporous silica particles also enables loading of larger antigen proteins. This was shown by Cha *et al.*, who successfully delivered the complete OVA protein in combination with a TLR-9 adjuvant by means of extra-large-pore MSNs.[82] We note that, in the latter study, antigen and adjuvant were both loaded *via* electrostatic interactions into randomly amine-functionalized particles without an additional capping system. This may cause uncontrolled release and therefore systemic activation or enhanced protein corona formation and thus rapid clearance of the particles before they reach DCs.[68] The spatially controlled synthesis of core−shell MSNs with a multifunctional capping system can overcome these obstacles. Future studies will show if MSN−R848 coloaded with antigen(s) not only leads to stronger DC activation but also enhances the cytotoxic T-cell responses *in vivo*.

CONCLUSIONS

MSNs hold considerable promise as a carrier system for the immune-stimulant R848. They display significant adjustability and flexibility, which allows for simultaneous delivery of adjuvant and antigen and the specific generation of an enhanced T-cell response. The pH-responsive system presented here thus shows great potential as a successful cancer vaccine, enabling enhanced and prolonged local immune activation and thus critically modifying the kinetics of small molecule immune-activating drugs.

METHODS

Materials. All reagents were purchased from commercial suppliers: tetraethyl orthosilicate (TEOS, Sigma-Aldrich, >98%), cetyltrimethylammonium chloride (CTAC, Fluka, 25 wt % in H_2O), triethanolamine (TEA, Sigma-Aldrich, 98%), triethoxyphenylsilane (PhTES, Sigma-Aldrich, 98%), 3-(triethoxysilyl)propylsuccinic anhydride (TEPSA, ABCR, 60−70%), 3,9-bis(3-aminopropyl)-2,4,8,10-tetraoxaspiro[5.5]-undecane (AK linker, TCI, ≥98%), biotin (Sigma-Aldrich, ≥99%), avidin, egg white (Merck Millipore, ≥10 units/mg protein), *N*-(3-(dimethylamino)propyl)-*N*-ethylcarbodiimide hydrochloride (EDC, Sigma-Aldrich, 97%), ammonium nitrate (Sigma-Aldrich, 99%), *N*-hydroxysulfosuccinimide sodium salt (sulfo-NHS, Sigma-Aldrich, 98%), ethanol (EtOH, Sigma-Aldrich, >99.5%), saline−sodium citrate buffer concentrate (SSC buffer (20×), Sigma-Aldrich), 2-morpholinoethanesulfonic acid hydrate (MES hydrate, Sigma-Aldrich, ≥99.5%), fluorescamine (Fluram, Sigma-Aldrich, ≥99%), TLR-7/8 agonist resiquimod (R848, Enzo, ≥98%), OVA 257−264 peptide (chicken egg albumin, Invivogen, ≥95%), 2-iminothiolane hydrochloride (Sigma-Aldrich, ≥98%), and α-maleimido-24(ethylene glycol)-ω-propionic acid succinimidyl ester (mal-dPEG(24)-NHS, Iris Biotech GmbH). All chemicals were used as received without further purification. Doubly distilled water from a Millipore system (Milli-Q Academic A10) was used for all synthesis and purification steps.

Preparation of MES Buffer (0.1 M, pH 5.5). 2-(*N*-Morpholino)-ethanesulfonic acid (MES, 9.76 g) was dissolved in 500 mL of water. The pH was adjusted to 5.5 using sodium hydroxide (1 M).

Synthesis Procedures. *Preparation of Core−Shell-Functionalized Colloidal Mesoporous Silica Nanoparticles (MSN−Ph_{in}−$COOH_{out}$).* Core−shell-functionalized MSNs were synthesized according to a slightly modified synthesis approach as previously reported.[35] In detail, a mixture of tetraethyl orthosilicate (TEOS, 1.62 g, 7.79 mmol) and triethoxyphenylsilane (PhTES, 0.45 g, 1.86 mmol) was added as a layer on top of triethanolamine (TEA, 14.3 g, 95.6 mmol) and heated without stirring at 90 °C for 20 min in a polypropylene reactor. Subsequently, a solution of cetyltrimethylammonium chloride (CTAC, 2.41 mL, 1.83 mmol, 25 wt % in H_2O) and ammonium fluoride (NH_4F, 100 mg, 2.7 mmol) in water (21.7 g, 1.21 mmol) preheated to 60 °C was quickly added and the reaction mixture vigorously stirred (700 rpm, 20 min) while cooling to room temperature. Afterward, four equal portions of TEOS (192.2 mg in total, 0.922 mmol) were added every 3 min, and the reaction mixture was allowed to stir for another 30 min at room temperature. In the end, TEOS (38.3 mg, 184 μmol) and 3-(triethoxysilyl)propylsuccinic anhydride (TEPSA, 56.2 mg, 184 μmol) were added, and the resulting mixture was allowed to stir overnight at room temperature. In the following, MSNs were collected by centrifugation (43,146 rcf, 20 min) and redispersed in absolute ethanol. Subsequent template extraction of the MSNs was performed in 100 mL of ethanolic solution, containing ammonium nitrate (NH_4NO_3, 2 g), under reflux heating at 90 °C for 45 min. After centrifugation (7179 rcf, 15 min) and redispersion in ethanol, the described extraction was performed a second time. Finally, the MSNs were collected by centrifugation (7179 rcf, 15 min) and washed with 100 mL of absolute ethanol, resulting in the sample MSN−Ph_{in}−$COOH_{out}$.

AK Linker Attachment (MSN−Ph_{in}−AK_{out}). Fifty milligrams of MSN−Ph_{in}−$COOH_{out}$ was collected by centrifugation (7179 rcf, 15 min) and redispersed in 70 mL of a 1:1 EtOH/HBSS buffer solution. Subsequently, EDC (20 μL, 114.4 μmol) was added under vigorous stirring of the particle solution. Ten minutes later, *N*-hydroxysulfosuccinimide sodium salt (sulfo-NHS, 2.6 mg, 12 μmol) was added and the reaction mixture allowed to stir five more minutes at room temperature. Afterward, the acetal linker 3,9-bis(3-aminopropyl)-2,4,8,10-tetraoxaspiro[5.5]undecane (AK linker, 917 μL (55 mg, 0.20 mmol) from stock solution with c = 60 mg/mL in 1:1 EtOH/HBSS mixture) was added dropwise to the solution, and the resulting mixture was allowed to stir overnight (700 rpm, room temperature). Particles were collected by centrifugation (7179 rcf, 15 min) and washed twice with absolute ethanol (50 mL).

Biotin Functionalization (MSN−Ph_{in}−$biotin_{out}$). Biotin (6 mg, 24.6 μmol) was dissolved in a DMSO/EtOH mixture (500 μL of DMSO, 2.5 mL of EtOH). Subsequently, EDC (6 μL, 34.3 μmol) was added under vigorous stirring, followed by sulfo-NHS (0.78 mg, 3.6 μmol). Then, 30 mg of MSN−Ph_{in}−AK_{out}, redispersed in 40 mL of ethanol, was added dropwise to the solution. The reaction mixture was allowed to react overnight (700 rpm, room temperature). Particles were collected by

https://dx.doi.org/10.1021/acsnano.0c08384
ACS Nano XXXX, XXX, XXX−XXX

centrifugation (7179 rcf, 15 min) and likewise washed twice with absolute ethanol (50 mL).

Avidin Coating (MSN–Ph_{in}–$avidin_{out}$). Two milligrams of MSN–Ph_{in}–$biotin_{out}$ was centrifuged (5500 rcf, 4 min, 15 °C) and redispersed in 400 μL of avidin solution (c = 10 mg/mL). The reaction mixture was allowed to react under dark and static conditions at room temperature overnight. The resulting particles (MSN–Ph_{in}–$avidin_{out}$) were extensively washed with SSC20x buffer (pH 7.0) and centrifuged (5500 rcf, 4 min, 15 °C).

Attachment of OVA Peptide to Avidin Cap (MSN–Ph_{in}–$OVAp_{out}$). A solution with 1 mg of MSN–Ph_{in}–$avidin_{out}$ was centrifuged (5500 rcf, 4 min, 15 °C), and the solid was redispersed in 500 μL of DPBS buffer. In the meantime, 2-iminothiolane hydrochloride (0.4 mg, 2.9 μmol) was added to a solution of 50 μL of OVA peptide (=OVAp = SIINFEKL; c = (OVAp-Stock) = 1 mg/mL in bidistilled water) in 450 μL of DPBS buffer. The mixture was allowed to react for 1 h at room temperature under static conditions. Afterward, the heterobifunctional PEG-linker mal-PEG(24)-NHS (0.6 mg, 430 μmol) was added, and the reaction mixture was allowed to react another hour at room temperature without stirring. The activated OVAp-PEG-linker was successively added to the MSN solution, and the mixture was allowed to react one more hour (static conditions). Subsequently, the OVAp-functionalized particles were washed three times with DPBS buffer (5500 rcf, 4 min, 15 °C).

Labeling of MSNs with Covalently Attached Atto Dyes. One milligram of MSN–SH_{in}–$biotin_{out}$ was redispersed in 1 mL of ethanol and 5 μL of Atto633-maleimide (or alternatively Atto488-mal) was added. The reaction mixture was allowed to react overnight at room temperature in the dark under static conditions. Subsequently, the labeled particles were washed three times with ethanol (1 mL of EtOH, 14,000 rpm, 5 min, room temperature) and one time with SSC20x buffer before avidin was added to the solution (as described above). Labeled particles were used for uptake and biodistribution studies.

Characterization of MSNs. Centrifugation was performed using a Sigma 3-30KS equipped with a fixed-angle rotor 12310 or an Eppendorf centrifuge (5430 for volumes up to 50 mL or 5418 for small volumes). Samples were investigated with a Tecnai G2 20 S-Twin transmission electron microscope operated at 200 kV with a bright-field detector. A droplet of the diluted MSN solution in absolute ethanol was dried on a carbon-coated copper grid at room temperature for several hours. Nitrogen sorption measurements were performed on a Quantachrome Instruments NOVA 4000e. In general, samples (15 mg each) were heated to 60 °C for 12 h in vacuum (10 mTorr) to outgas them before nitrogen sorption measurements. MSN–Ph_{in}–$avidin_{out}$ was the only sample which was outgassed at room temperature for 12 h in vacuum (10 mTorr) to void damage of the protein. Subsequent nitrogen sorption measurements were performed at 77 K. Pore size and pore volume were calculated by a NLDFT equilibrium model of N_2 on silica, based on the adsorption branch of the isotherms. Pore volumes were calculated only up to a pore size of 8 nm to avoid contributions of interparticle textural porosity. The specific surface area of the samples was determined with a BET model applied in the range of 0.05–0.20 p/p_0. Dynamic light scattering measurements were performed on a Malvern Zetasizer-Nano instrument equipped with a 4 mW He–Ne laser (633 nm) and an avalanche photodiode. To determine the hydrodynamic radius of the particles, 100 μL of an ethanolic MSN suspension (~10 mg/mL) was diluted with 3 mL of ethanol prior to the DLS measurement. The sample MSN–Ph_{in}–$avidin_{out}$ was measured in water, at similar concentrations. Zeta-potential measurements of the samples were performed on a Malvern Zetasizer-Nano instrument equipped with a 4 mW He–Ne laser (633 nm) and an avalanche photodiode using the add-on Zetasizer titration system (MPT-2) (based on diluted NaOH and HCl as titrants). For this purpose, particles were diluted in 10 mL of bidistilled water to achieve a final MSN concentration of 0.1 mg/mL.

Thermogravimetric analysis was performed on a Netzsch STA 440 C TG/DSC with a heating rate of 10 K/min in a stream of synthetic air of about 25 mL/min. The mass was normalized to 100% at 130 °C for all samples to exclude the influence of solvent desorption. A Thermo Scientific Nicolet iN10 IR-microscope was used to record infrared spectra of dried sample powders in reflection–absorption mode with a liquid-N_2 cooled MCT-A detector. UV–vis measurements with 2 μL of the samples were performed on a NanoDrop 2000c spectrometer from Thermo Scientific Fisher. Time-based fluorescence release experiments were performed at 37 °C on a PTI spectrofluorometer equipped with a xenon short arc lamp (UXL-75XE USHIO) and a photomultiplier detection system (model 810/814) with λ_{ex} = 323 nm and λ_{em} = 342 nm. Emission scans of fluorescent samples and corresponding calibration curves were measured at room temperature with λ_{ex} = 323 nm and λ_{em} = 335–355 nm.

Fluram Assay. The 2.5 mg particles from ethanolic solution were washed one time with MeOH and subsequently redispersed in 2 mL of MeOH. Subsequently, 1 mL of a freshly prepared Fluram solution (6.957 mg in 5 mL of MeOH, 5 mM) was added and the mixture vigorously shaken and vortexed for 2 min. Immediately afterward, samples were measured with fluorescence spectroscopy (λ_{ex} = 420 nm, λ_{em} = 440–540 nm).

Release Experiments. *Drug Loading (MSN–R848).* Two milligrams of MSN–Ph_{in}–$biotin_{out}$ was washed once with SSC20x buffer, followed by redispersion in 500 μL of R848 stock solution (consisting of 50 μL resiquimod (c = 10 mg/mL) in 450 μL of SSC20x buffer (pH 7.0)), yielding an overall drug concentration of 1 mg/mL in the loading solution. The particles were shaken for 1 h (thermoshaker, 600 rpm, room temperature), centrifuged, washed five times with SSC20x buffer, and redispersed in 400 μL of avidin solution (c = 10 mg/mL in SSC20x buffer) to trigger closure of the pores by biotin–avidin complex formation. The resulting particles (MSN–R848) were extensively washed with SSC20x buffer (pH 7.0) until no absorption at λ = 320 nm was detected in the supernatant. For *in vivo* experiments, MSNs were redispersed in SSC20x buffer at a concentration of 10 mg/mL.

Time-Based Fluorescence Release Experiments in Cuvette. A sample of 1 mg of R848-loaded MSNs redispersed in 1 mL of SSC20x buffer was split into two and centrifuged (5500 rcf, 4 min, 15 °C). One half (0.5 mg MSNs) was redispersed again in 200 μL of SSC20x buffer (pH 7.0), the other half in 200 μL of MES buffer (pH 5.5). Afterward, the MSNs (200 μL each) were transferred to custom-made caps which were sealed with a dialysis membrane (ROTH Visking type 8/32, MWCO 14 000 g/mol) and put on top of a disposable PMMA cuvette (UV grade). The cutoff molecular weight of the dialysis membrane is too low for MSNs and the detached biotin–avidin complex, meaning only released resiquimod can diffuse through the membrane to be measured in the cuvette. The pH-dependent cargo release was measured at 37 °C for 60 h (λ_{ex} = 323 nm, λ_{em} = 342 nm).

Quantification of Released Resiquimod/R848. To determine the amount of released resiquimod, samples were allowed to cool to room temperature after the time-based release. Subsequently, emission scans were performed at 22 °C (λ_{ex} = 323 nm, λ_{em} = 335–355 nm). To enable quantification (calibration), emission scans of concentration ranges of resiquimod in the respective buffers were measured under the same condition as mentioned above. Results were plotted and linearly fitted with Origin Pro 9.0 to be able to calculate the amounts of resiquimod released.

Supernatant/Loading Control with UV–Vis (Nanodrop). To follow the time-dependent loading of resiquimod, supernatants were measured during the loading process with Nanodrop (2 μL sample, blank: corresponding buffer). Furthermore, the successful washing procedure was monitored by measuring the decreasing optical absorption of the washing supernatants.

Biological Assays. *Uptake of MSNs by Antigen-Presenting Cells.* J774A.1 macrophages (ATCC, TIB-67) were plated at a concentration of 5 × 10^4 cells/well on a Lab-Tek chamber plate (Nunc) in high glucose (4.5 g/L) DMEM (Biowest) supplemented with 10% FBS (MP Biomedicals), 2 mM L-glutamine (Corning, Fisher Scientific), 1 mM sodium pyruvate (Gibco), and 0.5% ciprofloxacin (Bayer). After overnight incubation at 37 °C, the cells were stained with LysoTracker (Blue DND-22, life technologies) for 1 h at a final concentration of 50 nM. Atto633-labeled MSNs (20 μg/mL) were then added directly onto the cells. Live cell imaging was performed using a confocal microscope (Zeiss LSM 710 Meta) with 63× magnification. The colocalization analysis Pearson's R was calculated with Fiji.

https://dx.doi.org/10.1021/acsnano.0c08384
ACS Nano XXXX, XXX, XXX–XXX

To assess uptake into primary cells, single cell suspensions from total spleen and lymph nodes were used. To obtain single cell suspensions from spleens, the tissue was mechanically disrupted and filtered through a 70 μm cell strainer (Corning). Erythrocytes were lysed using Pharm Lyse buffer (BD Biosciences). To attain single cell suspensions from lymph nodes, the tissue was cut and digested in RPMI-1640 (Gibco) supplemented with 2% FBS (MP Biomedicals), 1× penicillin/streptomycin (Gibco), 10 mM HEPES (Gibco), 2 mM calcium chloride (Acros Organics), 3 mg/mL collagenase IV (Worthington), and 200 U/mL DNase I (Worthington) at 37 °C for 20−30 min on a shaker. After digestion, the suspension was filtered through a 70 μm cell strainer (Corning). Splenocytes or lymph node cells were cultured in RPMI-1640 (Gibco), 10% FBS (MP Biomedicals), 2 mM L-glutamine (Gibco), 1× penicillin/streptomycin (Gibco), 1 mM sodium pyruvate (Gibco), 1× nonessential amino acids (Gibco), and 50 μM 2-mercaptoethanol (Gibco) on a 96-well flat bottom plate (Greiner) at a density of 5×10^5 cells/well. MSNs were added at concentrations between 1 and 200 μg/mL to the cells and incubated overnight before analysis by flow cytometry.

Dendritic Cell Activation Assay. Bone-marrow-derived dendritic cells were generated as previously described with the only difference that cells were split (1 to 2) at day 3.[83] On day 6, BMDCs were seeded on a 96-well flat bottom plate (Greiner) at a density of 1×10^5 cells/well and stimulated with different concentrations of R848-loaded MSNs, free R848 (Enzolive), or supernatants coming from the spun down MSN formulations. The amount of MSN−R848 or MSN−R848−OVAp was calculated with the help of R848 release measurements. Due to minor variations of R848 released per milligram MSN between different batches, the amount of MSN−R848 or MSN−R848−OVAp was adjusted for every experiment to reach an equimolar amount between loaded or free R848. For some experiments, the endolysosomal acidification inhibitor chloroquine (Invivogen, 100 μM) was added 30 min before addition of the stimulants. After 18−24 h, cells and culture supernatants were collected and analyzed by flow cytometry and ELISA, respectively.

T-Cell Proliferation Assay in Vitro. BMDCs were generated as described in the previous section and seeded at a density of 1×10^5 cells/well on a 96-well flat bottom plate. Cells were then stimulated with different concentrations of R848- and/or SIINFEKL-loaded MSNs for 24 h. SIINFEKL-specific $CD8^+$ T cells were isolated from spleens coming from OT-I transgenic mice. For purification of $CD8^+$ T cells, magnetic-associated cell sorting (MACS) with the $CD8a^+$ T-cell isolation kit (Miltenyi) was performed according to manufacturer's protocol. T cells were stained with 0.5 μM CFSE (5-(and 6)-carboxyfluorescein diacetate succinimidyl ester, Biolegend) for 10 min at room temperature before adding them onto the stimulated BMDCs at a density of 1×10^5 cells/well in very low endotoxin RPMI-1640 (Biochrom), 10% FBS (MP Biomedicals), 2 mM L-glutamine (Gibco), 1× penicillin/streptomycin (Gibco), 1 mM sodium pyruvate (Gibco), 1× nonessential amino acids (Gibco), and 50 μM 2-mercaptoethanol (Gibco). CFSE passively diffuses into cells and covalently links to intracellular molecules, which leads to its dilution with each cell division. T-cell proliferation (defined by a lower presence of CFSE) was analyzed by flow cytometry after 2−3 days.

Quantification of Cytokines. Cell supernatants and serum were collected and analyzed for cytokine secretion by enzyme-linked immunosorbent assay (IL-6, TNFα, IL-12p40 ELISA kits, Biolegend) according to the manufacturer's protocol.

Flow Cytometry. Cell suspensions were stained in PBS (Gibco) with 0.5% BSA (Pan Biotech) and 0.5 mM EDTA (Promega). Fc receptor block (TruStain FCX anti-mouse CD16/32), fluorochrome-coupled antibodies against the surface antigens CD3, CD4, CD8, CD11b, CD11c, CD19, CD25, CD45, CD69, CD80, CD86, CD103, MHCI, MHCII, and appropriate isotype controls were all purchased from Biolegend. To assess cell death, a Zombie dye (Biolegend) was used according to the manufacturer's protocol. Cells were acquired on the flow cytometer NovoCyte (Acea Biosciences) and analyzed using the software FlowJo V10. In all graphs, dead cells were excluded with the help of the Zombie dye.

LC-MS/MS Measurements of R848 in Serum. Concentrations of R848 in mice serum were determined using a fully validated LC-MS/MS method. The instrument consisted of an Agilent HP1100 liquid chromatography coupled to an API 4000 triple quadrupole mass spectrometer (AB Sciex, Concord, ON, Canada) controlled by Analyst 1.6.1 software. The mass spectrometer was operated in the multiple reaction monitoring (MRM) mode with positive electrospray ionization. The MRM transitions were 315.4 → 251.0 and 330.1 → 295.1 with a dwell time of 100 ms for R848 and IS (midazolam-d_4), respectively. Other MS parameters were as follows: collision gas (8), curtain gas (30), ion source gas 1 (30), gas 2 (40), ion spray voltage (5000), and source temperature (600 °C). Chromatography was performed on a Phenomenex Kinetex C18 analytical column (50 mm × 2.1 mm, 2.6 μm; Torrance, CA, USA) preceded by a KrudKatcher ultra in-line filter, 0.5 μm. Flow rate was 0.4 mL/min using gradient of formic acid 0.1% in water (solvent A) and acetonitrile with formic acid 0.1% (solvent B). The method was fully validated with a quantitation limit of 1 ng/mL. Plasma samples (100 μL) were spiked with 50 μL of IS (50 ng/mL of midazolam-d_4) and basified with 100 μL of NaOH 0.5 M. After the addition of 0.5 mL of hexane/ethyl acetate (50−50 v/v), the mixture was shaken for 15 min. After centrifugation (1300g, 5 min), the tubes were stored in a freezer (−80 °C) until the aqueous phase froze (30 min) and the upper organic layer was saved. After evaporation, residues were reconstituted in 100 μL of formic acid 0.1% acetonitrile (80−20 v/v) and 10 μL was injected onto the HPLC system. Along with the experimental samples, quality control (QC) and standards samples, prepared using blank plasma spiked with R848, covering the expected concentration range were processed. The standard curves were obtained by weighted least-squares regression (weighting = $1/X$) of the measured peak area *versus* the analyte concentrations. The standard curves were used to calculate concentrations of the analytes in experimental and QC samples. The pharmacokinetics parameters (half-life and AUC) were calculated with the software Phoenix WinNonlin (Version 6.1) from Certara.

MSN Biodistribution and Activation Studies in Mice. To assess the biodistribution of the particles in different organs, mice were injected subcutaneously (s.c.) in the right hind limb with 1 mg of Atto633-labeled MSNs in a volume of 100 μL. For activation studies, R848-loaded MSNs or free R848 (10 μg per mouse) were injected s.c. in the right hind limb. The amount of MSN−R848 to be injected was calculated with the help of R848 release measurements and adjusted for every batch to reach 10 μg of R848 per mouse. For the control groups 100 μL of PBS or unloaded MSNs was injected. After 3 or 24 h, blood, lymph nodes, and spleens were collected and organs were processed as described in previous sections to obtain single cell suspensions. The cells were then analyzed by flow cytometry. Blood samples were left to coagulate at room temperature for a minimum of 1−2 h before centrifuging them at a maximum speed for 30 min. The serum was then collected and stored at −20 °C until further analysis by ELISA and LC-MS/MS.

Mice. Female C57Bl/6 and OT-I mice (purchased from Charles River, France) were housed under specific pathogen-free conditions and were 6−16 weeks of age at the time of the experiment. All animal studies were conducted in accordance with local regulations.

Statistics. All data sets are presented as mean + standard deviation. For comparison between just two data sets, the two-tailed t test was used. For multiple statistical comparison, the one- or two-way ANOVA test with either Tukey or Sidak post-test was applied. Significance was set at p values of $p < 0.05$, $p < 0.01$, $p < 0.001$, and $p < 0.0001$ and was then indicated with an asterisk (*, **, ***, and **** or ns = not significant). All statistical calculations were performed with GraphPad Prism (version 8).

ASSOCIATED CONTENT

Supporting Information

The Supporting Information is available free of charge at https://pubs.acs.org/doi/10.1021/acsnano.0c08384.

Additional characterization and description of the MSN functionalization process; detailed description of the

https://dx.doi.org/10.1021/acsnano.0c08384
ACS Nano XXXX, XXX, XXX−XXX

R848 loading optimization; uptake and toxicity of MSNs in splenocytes, macrophages, and BMDCs; impact of an endolysosomal acidification inhibitor on MSN−R848 functionality; stability of MSN−R848 in different media; activation of BMDCs by MSN−R848−OVAp and gating strategy for *in vitro* T-cell proliferation assay; lymph node scheme in a mouse; gating strategy for *in vivo* activation studies; additional information on DC and B cell activation in lymphoid organs; cytokine quantification in the serum of mice (PDF)

Video of MSN uptake in macrophages (AVI)

AUTHOR INFORMATION

Corresponding Authors

Thomas Bein − *Department of Chemistry and Center for NanoScience (CeNS), Ludwig-Maximilians-Universität (LMU) München, 81377 Munich, Germany;* orcid.org/0000-0001-7248-5906; Email: bein@lmu.de

Carole Bourquin − *Institute of Pharmaceutical Sciences of Western Switzerland, University of Geneva, 1211 Geneva, Switzerland; School of Pharmaceutical Sciences and Department of Anaesthesiology, Pharmacology, Intensive Care and Emergency Medicine, University of Geneva, 1211 Geneva, Switzerland;* orcid.org/0000-0003-3862-4583; Email: carole.bourquin@unige.ch

Authors

Julia Wagner − *Institute of Pharmaceutical Sciences of Western Switzerland, University of Geneva, 1211 Geneva, Switzerland; School of Pharmaceutical Sciences, University of Geneva, 1211 Geneva, Switzerland;* orcid.org/0000-0002-5019-6932

Dorothée Gößl − *Department of Chemistry and Center for NanoScience (CeNS), Ludwig-Maximilians-Universität (LMU) München, 81377 Munich, Germany;* orcid.org/0000-0003-4125-1706

Natasha Ustyanovska − *Department of Chemistry and Center for NanoScience (CeNS), Ludwig-Maximilians-Universität (LMU) München, 81377 Munich, Germany;* orcid.org/0000-0003-3783-7587

Mengyao Xiong − *Department of Chemistry and Center for NanoScience (CeNS), Ludwig-Maximilians-Universität (LMU) München, 81377 Munich, Germany;* orcid.org/0000-0001-8425-5200

Daniel Hauser − *Adolphe Merkle Institute, University of Fribourg, 1700 Fribourg, Switzerland;* orcid.org/0000-0003-2148-5820

Olga Zhuzhgova − *Department of Chemistry and Center for NanoScience (CeNS), Ludwig-Maximilians-Universität (LMU) München, 81377 Munich, Germany*

Sandra Hočevar − *Institute of Pharmaceutical Sciences of Western Switzerland, University of Geneva, 1211 Geneva, Switzerland; School of Pharmaceutical Sciences, University of Geneva, 1211 Geneva, Switzerland;* orcid.org/0000-0002-9770-8229

Betül Taskoparan − *Institute of Pharmaceutical Sciences of Western Switzerland, University of Geneva, 1211 Geneva, Switzerland; School of Pharmaceutical Sciences, University of Geneva, 1211 Geneva, Switzerland;* orcid.org/0000-0003-1890-1547

Laura Poller − *Department of Chemistry and Center for NanoScience (CeNS), Ludwig-Maximilians-Universität (LMU) München, 81377 Munich, Germany*

Stefan Datz − *Department of Chemistry and Center for NanoScience (CeNS), Ludwig-Maximilians-Universität (LMU) München, 81377 Munich, Germany*

Hanna Engelke − *Department of Chemistry and Center for NanoScience (CeNS), Ludwig-Maximilians-Universität (LMU) München, 81377 Munich, Germany;* orcid.org/0000-0001-9529-9436

Youssef Daali − *Institute of Pharmaceutical Sciences of Western Switzerland, University of Geneva, 1211 Geneva, Switzerland; School of Pharmaceutical Sciences, University of Geneva, 1211 Geneva, Switzerland*

Complete contact information is available at: https://pubs.acs.org/10.1021/acsnano.0c08384

Author Contributions

⊗J.W., D.G., T.B., and C.B. contributed equally to this work. J.W. and D.G. participated in the design of the study. The nanoparticle synthesis was performed and optimized by D.G., N.U., S.D., M.X., O.Z., and L.P. Characterization and optimization of the carrier system as well as in cuvette stability, loading and release, and quantification measurements were performed and interpreted by D.G. The live cell imaging experiment was performed by D.H. The *in vitro* toxicity, uptake, immune activation, and T-cell proliferation studies were performed and interpreted by J.W. The *in vivo* biodistribution, toxicity, and activation studies were performed and interpreted by J.W.; S.H. and B.T. participated in the *in vivo* experiments. Y.D. performed the LC-MS/MS serum measurements. H.E. was involved as an expert advisor and helped guide the study. C.B. and T.B. designed and guided the study. The manuscript was written by J.W., D.G., C.B., and T.B., with contributions from all authors. All authors have given approval to the final version of the manuscript.

Notes

The authors declare no competing financial interest.

ACKNOWLEDGMENTS

We are grateful to Inès Mottas for her advice. We thank Steffen Schmidt for the TEM images. D.G., N.U., M.X., O.Z., L.P., S.D., H.E., and T.B. thank the German Research Foundation (DFG, SFB 1032, B05), the Center for NanoScience (CeNS) and the Nanosystems Initiative Munich (NIM) for financial support. J.W., B.T., S.H., and C.B. thank the Swiss National Science Foundation (projects 156372 and 182317) for financial support.

REFERENCES

(1) Couzin-Frankel, J. Breakthrough of the Year 2013. Cancer Immunotherapy. *Science* **2013**, *342*, 1432−3.

(2) Chen, D. S.; Mellman, I. Oncology Meets Immunology: The Cancer-Immunity Cycle. *Immunity* **2013**, *39*, 1−10.

(3) Smith, M.; Garcia-Martinez, E.; Pitter, M. R.; Fucikova, J.; Spisek, R.; Zitvogel, L.; Kroemer, G.; Galluzzi, L. Trial Watch: Toll-Like Receptor Agonists in Cancer Immunotherapy. *Oncoimmunology* **2018**, *7*, No. e1526250.

(4) Geisse, J.; Caro, I.; Lindholm, J.; Golitz, L.; Stampone, P.; Owens, M. Imiquimod 5% Cream for the Treatment of Superficial Basal Cell Carcinoma: Results from Two Phase III, Randomized, Vehicle-Controlled Studies. *J. Am. Acad. Dermatol.* **2004**, *50*, 722−33.

(5) Dockrell, D. H.; Kinghorn, G. R. Imiquimod and Resiquimod as Novel Immunomodulators. *J. Antimicrob. Chemother.* **2001**, *48*, 751−5.

(6) Dowling, D. J. Recent Advances in the Discovery and Delivery of TLR7/8 Agonists as Vaccine Adjuvants. *Immunohorizons* **2018**, *2*, 185−197.

(7) Rook, A. H.; Gelfand, J. M.; Wysocka, M.; Troxel, A. B.; Benoit, B.; Surber, C.; Elenitsas, R.; Buchanan, M. A.; Leahy, D. S.; Watanabe, R.; Kirsch, I. R.; Kim, E. J.; Clark, R. A. Topical Resiquimod Can Induce Disease Regression and Enhance T-Cell Effector Functions in Cutaneous T-Cell Lymphoma. *Blood* **2015**, *126*, 1452−61.
(8) Goldstein, D.; Hertzog, P.; Tomkinson, E.; Couldwell, D.; McCarville, S.; Parrish, S.; Cunningham, P.; Newell, M.; Owens, M.; Cooper, D. A. Administration of Imiquimod, an Interferon Inducer, in Asymptomatic Human Immunodeficiency Virus-Infected Persons to Determine Safety and Biologic Response Modification. *J. Infect. Dis.* **1998**, *178*, 858−61.
(9) Lynn, G. M.; Laga, R.; Darrah, P. A.; Ishizuka, A. S.; Balaci, A. J.; Dulcey, A. E.; Pechar, M.; Pola, R.; Gerner, M. Y.; Yamamoto, A.; Buechler, C. R.; Quinn, K. M.; Smelkinson, M. G.; Vanek, O.; Cawood, R.; Hills, T.; Vasalatiy, O.; Kastenmuller, K.; Francica, J. R.; Stutts, L.; et al. *in Vivo* Characterization of the Physicochemical Properties of Polymer-Linked TLR Agonists That Enhance Vaccine Immunogenicity. *Nat. Biotechnol.* **2015**, *33*, 1201−10.
(10) Thomas, S. N.; Vokali, E.; Lund, A. W.; Hubbell, J. A.; Swartz, M. A. Targeting the Tumor-Draining Lymph Node with Adjuvanted Nanoparticles Reshapes the Anti-Tumor Immune Response. *Biomaterials* **2014**, *35*, 814−24.
(11) Rueda, F.; Eich, C.; Cordobilla, B.; Domingo, P.; Acosta, G.; Albericio, F.; Cruz, L. J.; Domingo, J. C. Effect of TLR Ligands Co-Encapsulated with Multiepitopic Antigen in Nanoliposomes Targeted to Human DCs *via* Fc Receptor for Cancer Vaccines. *Immunobiology* **2017**, *222*, 989−997.
(12) Rahimian, S.; Fransen, M. F.; Kleinovink, J. W.; Christensen, J. R.; Amidi, M.; Hennink, W. E.; Ossendorp, F. Polymeric Nanoparticles for Co-Delivery of Synthetic Long Peptide Antigen and Poly IC as Therapeutic Cancer Vaccine Formulation. *J. Controlled Release* **2015**, *203*, 16−22.
(13) Rosalia, R. A.; Cruz, L. J.; van Duikeren, S.; Tromp, A. T.; Silva, A. L.; Jiskoot, W.; de Gruijl, T.; Lowik, C.; Oostendorp, J.; van der Burg, S. H.; Ossendorp, F. CD40-Targeted Dendritic Cell Delivery of PLGA-Nanoparticle Vaccines Induce Potent Anti-Tumor Responses. *Biomaterials* **2015**, *40*, 88−97.
(14) Bulbake, U.; Doppalapudi, S.; Kommineni, N.; Khan, W. Liposomal Formulations in Clinical Use: An Updated Review. *Pharmaceutics* **2017**, *9*, 12.
(15) Schwendener, R. A. Liposomes as Vaccine Delivery Systems: A Review of the Recent Advances. *Ther. Adv. Vaccines* **2014**, *2*, 159−82.
(16) Mahjub, R.; Jatana, S.; Lee, S. E.; Qin, Z.; Pauli, G.; Soleimani, M.; Madadi, S.; Li, S. D. Recent Advances in Applying Nanotechnologies for Cancer Immunotherapy. *J. Controlled Release* **2018**, *288*, 239−263.
(17) Tabatabaei Mirakabad, F. S.; Nejati-Koshki, K.; Akbarzadeh, A.; Yamchi, M. R.; Milani, M.; Zarghami, N.; Zeighamian, V.; Rahimzadeh, A.; Alimohammadi, S.; Hanifehpour, Y.; Joo, S. W. PLGA-Based Nanoparticles as Cancer Drug Delivery Systems. *Asian Pac J. Cancer Prev* **2014**, *15*, 517−35.
(18) Zupančič, E.; Silva, J.; Videira, M. A.; Moreira, J. N.; Florindo, H. F. Development of a Novel Nanoparticle-Based Therapeutic Vaccine for Breast Cancer Immunotherapy. *Procedia Vaccinol.* **2014**, *8*, 62−67.
(19) Kim, H.; Niu, L.; Larson, P.; Kucaba, T. A.; Murphy, K. A.; James, B. R.; Ferguson, D. M.; Griffith, T. S.; Panyam, J. Polymeric Nanoparticles Encapsulating Novel TLR7/8 Agonists as Immunostimulatory Adjuvants for Enhanced Cancer Immunotherapy. *Biomaterials* **2018**, *164*, 38−53.
(20) Widmer, J.; Thauvin, C.; Mottas, I.; Nguyen, V. N.; Delie, F.; Allemann, E.; Bourquin, C. Polymer-Based Nanoparticles Loaded with a TLR7 Ligand to Target the Lymph Node for Immunostimulation. *Int. J. Pharm.* **2018**, *535*, 444−451.
(21) Ilyinskii, P. O.; Roy, C. J.; O'Neil, C. P.; Browning, E. A.; Pittet, L. A.; Altreuter, D. H.; Alexis, F.; Tonti, E.; Shi, J.; Basto, P. A.; Iannacone, M.; Radovic-Moreno, A. F.; Langer, R. S.; Farokhzad, O. C.; von Andrian, U. H.; Johnston, L. P.; Kishimoto, T. K. Adjuvant-Carrying Synthetic Vaccine Particles Augment the Immune Response to Encapsulated Antigen and Exhibit Strong Local Immune Activation without Inducing Systemic Cytokine Release. *Vaccine* **2014**, *32*, 2882−95.
(22) Oliveira, C. L.; Veiga, F.; Varela, C.; Roleira, F.; Tavares, E.; Silveira, I.; Ribeiro, A. J. Characterization of Polymeric Nanoparticles for Intravenous Delivery: Focus on Stability. *Colloids Surf., B* **2017**, *150*, 326−333.
(23) Hočevar, S.; Milosevic, A.; Rodriguez-Lorenzo, L.; Ackermann-Hirschi, L.; Mottas, I.; Petri-Fink, A.; Rothen-Rutishauser, B.; Bourquin, C.; Clift, M. J. D. Polymer-Coated Gold Nanospheres Do Not Impair the Innate Immune Function of Human B Lymphocytes *in Vitro*. *ACS Nano* **2019**, *13*, 6790−6800.
(24) Mottas, I.; Bekdemir, A.; Cereghetti, A.; Spagnuolo, L.; Yang, Y. S.; Muller, M.; Irvine, D. J.; Stellacci, F.; Bourquin, C. Amphiphilic Nanoparticle Delivery Enhances the Anticancer Efficacy of a TLR7 Ligand *via* Local Immune Activation. *Biomaterials* **2019**, *190*−*191*, 111−120.
(25) Havel, H. A. Where Are the Nanodrugs? An Industry Perspective on Development of Drug Products Containing Nanomaterials. *AAPS J.* **2016**, *18*, 1351−1353.
(26) Bobo, D.; Robinson, K. J.; Islam, J.; Thurecht, K. J.; Corrie, S. R. Nanoparticle-Based Medicines: A Review of FDA-Approved Materials and Clinical Trials to Date. *Pharm. Res.* **2016**, *33*, 2373−87.
(27) Zhang, X. Gold Nanoparticles: Recent Advances in the Biomedical Applications. *Cell Biochem. Biophys.* **2015**, *72*, 771−5.
(28) Argyo, C.; Weiss, V.; Bräuchle, C.; Bein, T. Multifunctional Mesoporous Silica Nanoparticles as a Universal Platform for Drug Delivery. *Chem. Mater.* **2014**, *26*, 435−451.
(29) Tarn, D.; Ashley, C. E.; Xue, M.; Carnes, E. C.; Zink, J. I.; Brinker, C. J. Mesoporous Silica Nanoparticle Nanocarriers: Biofunctionality and Biocompatibility. *Acc. Chem. Res.* **2013**, *46*, 792−801.
(30) Möller, K.; Bein, T. Degradable Drug Carriers: Vanishing Mesoporous Silica Nanoparticles. *Chem. Mater.* **2019**, *31*, 4364−4378.
(31) Bunker, B. C. Molecular Mechanisms for Corrosion of Silica and Silicate-Glasses. *J. Non-Cryst. Solids* **1994**, *179*, 300−308.
(32) Vallet-Regi, M.; Colilla, M.; Izquierdo-Barba, I.; Manzano, M. Mesoporous Silica Nanoparticles for Drug Delivery: Current Insights. *Molecules* **2018**, *23*, 47.
(33) Croissant, J. G.; Fatieiev, Y.; Khashab, N. M. Degradability and Clearance of Silicon, Organosilica, Silsesquioxane, Silica Mixed Oxide, and Mesoporous Silica Nanoparticles. *Adv. Mater.* **2017**, *29*, 1604634.
(34) Heidegger, S.; Gößl, D.; Schmidt, A.; Niedermayer, S.; Argyo, C.; Endres, S.; Bein, T.; Bourquin, C. Immune Response to Functionalized Mesoporous Silica Nanoparticles for Targeted Drug Delivery. *Nanoscale* **2016**, *8*, 938−48.
(35) Cauda, V.; Schlossbauer, A.; Kecht, J.; Zurner, A.; Bein, T. Multiple Core-Shell Functionalized Colloidal Mesoporous Silica Nanoparticles. *J. Am. Chem. Soc.* **2009**, *131*, 11361−70.
(36) Schlossbauer, A.; Kecht, J.; Bein, T. Biotin-Avidin as a Protease-Responsive Cap System for Controlled Guest Release from Colloidal Mesoporous Silica. *Angew. Chem., Int. Ed.* **2009**, *48*, 3092−5.
(37) Datz, S.; Argyo, C.; Gattner, M.; Weiss, V.; Brunner, K.; Bretzler, J.; von Schirnding, C.; Torrano, A. A.; Spada, F.; Vrabel, M.; Engelke, H.; Bräuchle, C.; Carell, T.; Bein, T. Genetically Designed Biomolecular Capping System for Mesoporous Silica Nanoparticles Enables Receptor-Mediated Cell Uptake and Controlled Drug Release. *Nanoscale* **2016**, *8*, 8101−10.
(38) Petronzelli, F.; Pelliccia, A.; Anastasi, A. M.; Lindstedt, R.; Manganello, S.; Ferrari, L. E.; Albertoni, C.; Leoni, B.; Rosi, A.; D'Alessio, V.; Deiana, K.; Paganelli, G.; De Santis, R. Therapeutic Use of Avidin Is Not Hampered by Antiavidin Antibodies in Humans. *Cancer Biother.Radiopharm.* **2010**, *25*, 563−70.
(39) Livnah, O.; Bayer, E. A.; Wilchek, M.; Sussman, J. L. Three-Dimensional Structures of Avidin and the Avidin-Biotin Complex. *Proc. Natl. Acad. Sci. U. S. A.* **1993**, *90*, 5076−5080.
(40) Pugliese, L.; Coda, A.; Malcovati, M.; Bolognesi, M. Three-Dimensional Structure of the Tetragonal Crystal Form of Egg-White Avidin in Its Functional Complex with Biotin at 2.7 A Resolution. *J. Mol. Biol.* **1993**, *231*, 698−710.

https://dx.doi.org/10.1021/acsnano.0c08384
ACS Nano XXXX, XXX, XXX−XXX

(41) DeLange, R. J.; Huang, T. S. Egg White Avidin. 3. Sequence of the 78-Residue Middle Cyanogen Bromide Peptide. Complete Amino Acid Sequence of the Protein Subunit. *J. Biol. Chem.* **1971**, *246*, 698−709.
(42) Cauda, V.; Engelke, H.; Sauer, A.; Arcizet, D.; Bräuchle, C.; Radler, J.; Bein, T. Colchicine-Loaded Lipid Bilayer-Coated 50 nm Mesoporous Nanoparticles Efficiently Induce Microtubule Depolymerization upon Cell Uptake. *Nano Lett.* **2010**, *10*, 2484−92.
(43) Huh, S.; Wiench, J. W.; Yoo, J. C.; Pruski, M.; Lin, V. S. Y. Organic Functionalization and Morphology Control of Mesoporous Silicas *via* a Co-Condensation Synthesis Method. *Chem. Mater.* **2003**, *15*, 4247−4256.
(44) Kecht, J.; Schlossbauer, A.; Bein, T. Selective Functionalization of the Outer and Inner Surfaces in Mesoporous Silica Nanoparticles. *Chem. Mater.* **2008**, *20*, 7207−7214.
(45) Kobler, J.; Moller, K.; Bein, T. Colloidal Suspensions of Functionalized Mesoporous Silica Nanoparticles. *ACS Nano* **2008**, *2*, 791−9.
(46) Baldwin, R. L. How Hofmeister Ion Interactions Affect Protein Stability. *Biophys. J.* **1996**, *71*, 2056−63.
(47) Cacace, M. G.; Landau, E. M.; Ramsden, J. J. The Hofmeister Series: Salt and Solvent Effects on Interfacial Phenomena. *Q. Rev. Biophys.* **1997**, *30*, 241−77.
(48) Deckwer, M. Hofmeistersche Reihen. In *Römpp Lexikon Biotechnologie Und Gentechnik*; Georg Thieme Verlag, 1999; p 376.
(49) Kniep, R. d.; Jaenicke, L.; Winter, R.; Fischer-Henningsen, D.; Lippert, B.; Gottschild, D.; Umbrecht, H.; Zahn, T. Wissenschaft Aktuell. *Chem. Unserer Zeit* **1996**, *30*, 46−51.
(50) Kennedy, R. M. Hydrophobic Chromatography. *Methods Enzymol.* **1990**, *182*, 339−43.
(51) Porath, J.; Sundberg, L.; Fornstedt, N.; Olsson, I. Salting-Out in Amphiphilic Gels as a New Approach to Hydrophobic Adsorption. *Nature* **1973**, *245*, 465−6.
(52) Franco, S.; Noureddine, A.; Guo, J.; Keth, J.; Paffett, M. L.; Brinker, C. J.; Serda, R. E. Direct Transfer of Mesoporous Silica Nanoparticles between Macrophages and Cancer Cells. *Cancers (Basel)* **2020**, *12*, 2892.
(53) Chou, C. C.; Chen, W.; Hung, Y.; Mou, C. Y. Molecular Elucidation of Biological Response to Mesoporous Silica Nanoparticles *in Vitro* and *in Vivo*. *ACS Appl. Mater. Interfaces* **2017**, *9*, 22235−22251.
(54) Rabinovitch, M. Professional and Non-Professional Phagocytes: An Introduction. *Trends Cell Biol.* **1995**, *5*, 85−7.
(55) Bourquin, C.; Pommier, A.; Hotz, C. Harnessing the Immune System to Fight Cancer with Toll-Like Receptor and Rig-I-Like Receptor Agonists. *Pharmacol. Res.* **2020**, *154*, 104192.
(56) Ducharme, J.; Farinotti, R. Clinical Pharmacokinetics and Metabolism of Chloroquine. Focus on Recent Advancements. *Clin. Pharmacokinet.* **1996**, *31*, 257−74.
(57) Ali, O. A.; Lewin, S. A.; Dranoff, G.; Mooney, D. J. Vaccines Combined with Immune Checkpoint Antibodies Promote Cytotoxic T-Cell Activity and Tumor Eradication. *Cancer Immunol. Res.* **2016**, *4*, 95−100.
(58) Lu, J.; Liong, M.; Li, Z.; Zink, J. I.; Tamanoi, F. Biocompatibility, Biodistribution, and Drug-Delivery Efficiency of Mesoporous Silica Nanoparticles for Cancer Therapy in Animals. *Small* **2010**, *6*, 1794−805.
(59) Hudson, S. P.; Padera, R. F.; Langer, R.; Kohane, D. S. The Biocompatibility of Mesoporous Silicates. *Biomaterials* **2008**, *29*, 4045−55.
(60) Eisenbarth, S. C. Dendritic Cell Subsets in T Cell Programming: Location Dictates Function. *Nat. Rev. Immunol.* **2019**, *19*, 89−103.
(61) Lucke, M.; Mottas, I.; Herbst, T.; Hotz, C.; Romer, L.; Schierling, M.; Herold, H. M.; Slotta, U.; Spinetti, T.; Scheibel, T.; Winter, G.; Bourquin, C.; Engert, J. Engineered Hybrid Spider Silk Particles as Delivery System for Peptide Vaccines. *Biomaterials* **2018**, *172*, 105−115.
(62) Hotz, C.; Treinies, M.; Mottas, I.; Rotzer, L. C.; Oberson, A.; Spagnuolo, L.; Perdicchio, M.; Spinetti, T.; Herbst, T.; Bourquin, C. Reprogramming of TLR7 Signaling Enhances Antitumor NK and Cytotoxic T Cell Responses. *Oncoimmunology* **2016**, *5*, No. e1232219.
(63) Nie, Y.; Yang; Trivett, A.; Han, Z.; Xin, H.; Chen, X.; Oppenheim, J. J. Development of a Curative Therapeutic Vaccine (Theravac) for the Treatment of Large Established Tumors. *Sci. Rep.* **2017**, *7*, 14186.
(64) Kitano, M.; Yamazaki, C.; Takumi, A.; Ikeno, T.; Hemmi, H.; Takahashi, N.; Shimizu, K.; Fraser, S. E.; Hoshino, K.; Kaisho, T.; Okada, T. Imaging of the Cross-Presenting Dendritic Cell Subsets in the Skin-Draining Lymph Node. *Proc. Natl. Acad. Sci. U. S. A.* **2016**, *113*, 1044−9.
(65) Tomura, M.; Hata, A.; Matsuoka, S.; Shand, F. H.; Nakanishi, Y.; Ikebuchi, R.; Ueha, S.; Tsutsui, H.; Inaba, K.; Matsushima, K.; Miyawaki, A.; Kabashima, K.; Watanabe, T.; Kanagawa, O. Tracking and Quantification of Dendritic Cell Migration and Antigen Trafficking between the Skin and Lymph Nodes. *Sci. Rep.* **2014**, *4*, 6030.
(66) Liu, R.; Zhang, Y.; Zhao, X.; Agarwal, A.; Mueller, L. J.; Feng, P. pH-Responsive Nanogated Ensemble Based on Gold-Capped Mesoporous Silica through an Acid-Labile Acetal Linker. *J. Am. Chem. Soc.* **2010**, *132*, 1500−1.
(67) Geisow, M. J.; Evans, W. H. pH in the Endosome. Measurements during Pinocytosis and Receptor-Mediated Endocytosis. *Exp. Cell Res.* **1984**, *150*, 36−46.
(68) van Rijt, S. H.; Bolukbas, D. A.; Argyo, C.; Wipplinger, K.; Naureen, M.; Datz, S.; Eickelberg, O.; Meiners, S.; Bein, T.; Schmid, O.; Stoeger, T. Applicability of Avidin Protein Coated Mesoporous Silica Nanoparticles as Drug Carriers in the Lung. *Nanoscale* **2016**, *8*, 8058−69.
(69) Oh, J. Y.; Kim, H. S.; Palanikumar, L.; Go, E. M.; Jana, B.; Park, S. A.; Kim, H. Y.; Kim, K.; Seo, J. K.; Kwak, S. K.; Kim, C.; Kang, S.; Ryu, J. H. Cloaking Nanoparticles with Protein Corona Shield for Targeted Drug Delivery. *Nat. Commun.* **2018**, *9*, 4548.
(70) Zhang, R.; Smith, J. D.; Allen, B. N.; Kramer, J. S.; Schauflinger, M.; Ulery, B. D. Peptide Amphiphile Micelle Vaccine Size and Charge Influence the Host Antibody Response. *ACS Biomater. Sci. Eng.* **2018**, *4*, 2463−2472.
(71) Irvine, D. J.; Hanson, M. C.; Rakhra, K.; Tokatlian, T. Synthetic Nanoparticles for Vaccines and Immunotherapy. *Chem. Rev.* **2015**, *115*, 11109−46.
(72) Kourtis, I. C.; Hirosue, S.; de Titta, A.; Kontos, S.; Stegmann, T.; Hubbell, J. A.; Swartz, M. A. Peripherally Administered Nanoparticles Target Monocytic Myeloid Cells, Secondary Lymphoid Organs and Tumors in Mice. *PLoS One* **2013**, *8*, No. e61646.
(73) Thauvin, C.; Widmer, J.; Mottas, I.; Hocevar, S.; Allemann, E.; Bourquin, C.; Delie, F. Development of Resiquimod-Loaded Modified PLA-Based Nanoparticles for Cancer Immunotherapy: A Kinetic Study. *Eur. J. Pharm. Biopharm.* **2019**, *139*, 253−261.
(74) Wilson, J. T.; Keller, S.; Manganiello, M. J.; Cheng, C.; Lee, C. C.; Opara, C.; Convertine, A.; Stayton, P. S. pH-Responsive Nanoparticle Vaccines for Dual-Delivery of Antigens and Immunostimulatory Oligonucleotides. *ACS Nano* **2013**, *7*, 3912−25.
(75) Duperret, E. K.; Liu, S.; Paik, M.; Trautz, A.; Stoltz, R.; Liu, X.; Ze, K.; Perales-Puchalt, A.; Reed, C.; Yan, J.; Xu, X.; Weiner, D. B. A Designer Cross-Reactive DNA Immunotherapeutic Vaccine That Targets Multiple MAGE-A Family Members Simultaneously for Cancer Therapy. *Clin. Cancer Res.* **2018**, *24*, 6015−6027.
(76) Liu, L. N.; Shivakumar, R.; Allen, C.; Fratantoni, J. C. Delivery of Whole Tumor Lysate into Dendritic Cells for Cancer Vaccination. *Methods Mol. Biol.* **2008**, *423*, 139−53.
(77) Chang, J. H.; Tsai, P. H.; Chen, W.; Chiou, S. H.; Mou, C. Y. Dual Delivery of SiRNA and Plasmid DNA Using Mesoporous Silica Nanoparticles to Differentiate Induced Pluripotent Stem Cells into Dopaminergic Neurons. *J. Mater. Chem. B* **2017**, *5*, 3012−3023.
(78) Zhao, Y.; Trewyn, B. G.; Slowing, II; Lin, V. S. Mesoporous Silica Nanoparticle-Based Double Drug Delivery System for Glucose-Responsive Controlled Release of Insulin and Cyclic Amp. *J. Am. Chem. Soc.* **2009**, *131*, 8398−400.

https://dx.doi.org/10.1021/acsnano.0c08384
ACS Nano XXXX, XXX, XXX−XXX

(79) Colilla, M.; Gonzalez, B.; Vallet-Regi, M. Mesoporous Silica Nanoparticles for the Design of Smart Delivery Nanodevices. *Biomater. Sci.* **2013**, *1*, 114−134.
(80) Slingluff, C. L., Jr.; Petroni, G. R.; Chianese-Bullock, K. A.; Smolkin, M. E.; Hibbitts, S.; Murphy, C.; Johansen, N.; Grosh, W. W.; Yamshchikov, G. V.; Neese, P. Y.; Patterson, J. W.; Fink, R.; Rehm, P. K. Immunologic and Clinical Outcomes of a Randomized Phase II Trial of Two Multipeptide Vaccines for Melanoma in the Adjuvant Setting. *Clin. Cancer Res.* **2007**, *13*, 6386−95.
(81) Sahin, U.; Tureci, O. Personalized Vaccines for Cancer Immunotherapy. *Science* **2018**, *359*, 1355−1360.
(82) Cha, B. G.; Jeong, J. H.; Kim, J. Extra-Large Pore Mesoporous Silica Nanoparticles Enabling Co-Delivery of High Amounts of Protein Antigen and Toll-Like Receptor 9 Agonist for Enhanced Cancer Vaccine Efficacy. *ACS Cent. Sci.* **2018**, *4*, 484−492.
(83) Helft, J.; Bottcher, J.; Chakravarty, P.; Zelenay, S.; Huotari, J.; Schraml, B. U.; Goubau, D.; Reis e Sousa, C. GM-CSF Mouse Bone Marrow Cultures Comprise a Heterogeneous Population of CD11c-(+)MHCII(+) Macrophages and Dendritic Cells. *Immunity* **2015**, *42*, 1197−211.

https://dx.doi.org/10.1021/acsnano.0c08384
ACS Nano XXXX, XXX, XXX−XXX